МИКРОТАЛАСНА ТЕХНИКА, ТЕХНОЛОГИЈЕ И СИСТЕМИ
/
MICROWAVE TECHNIQUE, TECHNOLOGIES AND SYSTEMS
(MT/MTI)

Modeling a Planar Circular Loop Antenna using Artificial Neural Networks

Ksenija Pešić[1], Zoran Stanković[2] and Nebojša Dončov[3]

Abstract - **In this paper we present a neural model for planar circular loop antenna based on multilayer perceptron (MLP) network. This model is realized by means of two coupled MLP networks which separately provide the resonant frequency and the minimum value of S_{11} parameter for specified antenna dimensions. The model is trained within the certain range of input parameters (radius of the antenna and the ratio of the radius and the width of loop antenna) that allows for design of planar circular loop antennas operating in the frequency band (500 - 2800) MHz.**

Keywords - **Circular Loop Antenna, Neural model, Neural network**

I. Introduction

Thanks to the development of microwave technology and the introduction of new technologies for conducting electromagnetic (EM) waves based on the use of printed planar structures, realized in microstrip and other similar techniques, printed antennas are being developed [1]. Simplicity production, small dimensions and weight, adaptability to the housings in which they are installed, low price, the ability to work in multiple frequency bands and large mechanical reliability are the features of printed antennas that justify their exceptional popularity and use [1,2]. All these advantages compensate for the disadvantages of printed antennas, such as low bandwidth and low gain, which are a consequence of the manufacturing technology.

Analytical techniques that solve the problems of propagation of EM waves, based on appropriate solutions of Maxwell's equations, are usually applicable for design of antennas with simple configuration. Since in general all antennas, including printed antennas, in real application can be very complex, the use of a numerical model of Maxwell's equations is the only alternative to analytical solutions. There is a large number of numerical techniques able to provide an efficient solution of EM problems, such as the finite element method (FEM) [3], the method of moments (MoM) [3,4], the split-step parabolic equation (SSPE) [4] method, the finite difference time-domain (FDTD) method [3,4] and the transmission line matrix (TLM) method [3,5]. However, these techniques are numerically demanding and careful programming is required in order to reduce time and memory consumption. During antenna design, it is usually necessary to consider a large number of geometrical parameters combinations in order to find a configuration that provides its optimal working performances in a frequency range of interest. Therefore, a process of designing antenna by using any of available numerical techniques can be even more time and memory demanding. Alternative to classical EM simulators may be a use of antenna models based on Artificial Neural Network (ANN) [6,7]. The process of developing a neural model can be also difficult and time consuming as for classical EM models, however when a neural model is successfully developed its speed exceeds the speeds of classical EM models [7-10]. Antenna modeling by using ANN has recently attracted more attention because of the convenience they offer [8-12]. The ANN approach proved to be good in [13,14] when it comes to modeling the resonant frequency and minimum values of S_{11} parameter of planar bowtie dipole and microwave slot antennas considered in [13] and [14], respectively.

In contrast to [13,14] where a model based on one multilayer perceptron (MLP) neural network with two outputs was used, in this paper we propose a neural model that consists of two MLP networks with one output. Each MLP network separately provides one antenna output parameter for input parameters of antenna. In this way, a dependence of each output parameter on input parameters is modeled independently allowing for better accuracy of neural model. The proposed model accuracy and efficiency is illustrated here on the example of design of planar circular loop antenna. Model is able to provide the resonant frequency and the minimum value of S_{11} parameter for specified circular loop antenna dimensions (radius of the antenna R and the ratio of the radius and the width of loop antenna k). Such designed antenna due to its radiation characteristics and the fact that it is soft, portable and very grateful for the extension of the frequency range because it can retain the low value of S_{11} parameter is a good candidate to be used in real-time locating system (RTLS). Nowadays, there is an increasing use of RTLS system that can accurately locate, track and manage assets, inventory or people and help companies make decisions based on the collected location data [15].

II. EM Model of the Planar Circular Loop Antenna

Fig. 1 shows the architecture of a planar circular loop antenna used for both the EM model and the neural model. The basic geometrical parameters are: R – radius of the antenna and d – the width of the loop antenna. Loop antennas are usually classified into two categories, electrically small (circumference is usually less than about one-tenth of a wavelength) and electrically large (circumference is about a free-space wavelength).

The input impedance of a small circular loop antenna made of a thin wire of radius a can be determined by an approximate formula [1]:

Ksenija Pešić[1], Zoran Stanković[2] and Nebojša Dončov[3] are with University of Niš, Faculty of Electronic Engineering, Aleksandra Medvedeva 14, 18000 Niš, Serbia, E-mails: [ksenija.pesic, zoran.stankovic, nebojsa.doncov]@elfak.ni.ac.rs

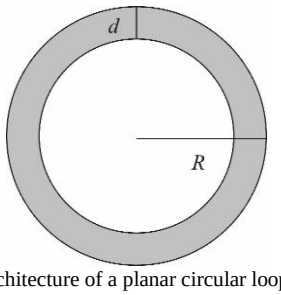

Fig. 1. Architecture of a planar circular loop antenna

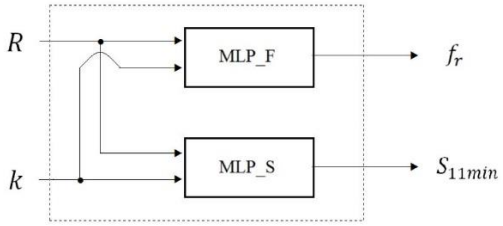

Fig. 2. The neural model of the planar circular loop antenna

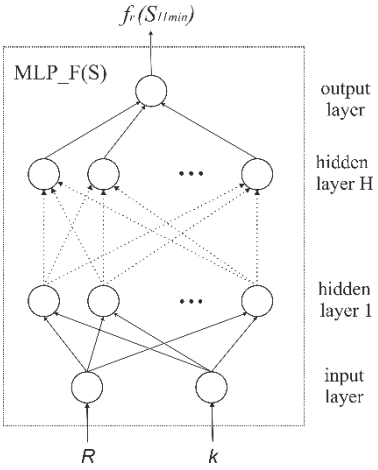

Fig. 3. Architecture of MLP_F(S) neural network

$$Z_{in} = \left(\frac{7.86 \cdot Rf}{10^8}\right)^4 + j \cdot 2\pi f \mu R \left(\ln\left(\frac{8R}{a}\right) - 1.75\right) \quad (1)$$

where f and μ represent the frequency of the signal and the magnetic permeability of the medium, respectively. When a circular loop antenna is made in a planar shape, its cross section should also be taken into account, so analyzes of frequency characteristics of antenna is much more complex and it cannot be performed with a direct usage Eq. (1). This equation will not give accurate results and instead EM simulator has to be used. Using the functions of the Toolbox Antenna in the MATLAB software environment [16], an EM model can be created in order to analyze the characteristics of this antenna. Antenna Toolbox uses the method of moments (MoM) to compute antenna properties such as input impedance, surface properties such as current and charge distribution, and field properties such as the near-field and far-field radiation pattern [16,17]. The basic function in Antenna Toolbox for creation of the circular antenna object is *loopCircular(Name,Value)*. This function creates a one wavelength circular loop antenna, with additional properties specified by one, or more name-value pair arguments [16]. Due to the small size of the antenna, the ratio of radius to width was used, and not the width of the antenna itself. This ratio is defined as $k = R / d$, where R is the radius of the loop and d is the width of the antenna. Accordingly, in the EM model, the variable parameters are the radius of the antenna and the previously defined ratio k. On the created loop antenna object we can use standard functions for network configuration in MoM method, antenna structure presentation, radiation pattern presentation, estimation of radiation in the plane of azimuth and elevation (*show*, *pattern*, *patternAzimuth*, *patternElevation*, *sparameters*) [16,17].

III. Neural Model of the Planar Circular Loop Antenna

The neural model of the planar circular loop antenna consists of two multilayer perceptron networks (MLP_F and MLP_S) and its architecture is shown in Fig.2. The main purpose of the model is to perform the mapping from a space of physical parameters of the antenna (radius of the antenna R and the ratio of the radius and the width of loop antenna k) to a space of antenna operating characteristics consisting of resonant frequency f_r

$$[f_r] = f_{MLP\_F}(R, k) \quad (2)$$

and minimum value of S_{11} parameter (value of S_{11} parameters at antenna resonant frequency - $S_{11\min}$)

$$[S_{11min}] = f_{MLP\_S}(R, k) \quad (3)$$

at the given feed line impedance (z_f =const). Neural networks MLP_S and MLP_F have the same architecture which is represented in Fig. 3.

In matrix representation, the neural model will have the vector of input variables $\mathbf{x} = [R \quad k]^T$. The vector of output variable in the MLP_F network will be $\mathbf{y} = [f_r]$, while in the MLP_S network the vector of the output variable is $\mathbf{y} = [S_{11min}]$. MLP neural network for both cases can be described by $\mathbf{y} = y(\mathbf{x}, W, B)$, where y is a network processing function, W is a set of connection weighting matrices $\mathbf{w}_i$, $W = \{\mathbf{w}_1, \mathbf{w}_2, \ldots \mathbf{w}_{H+1}\}$ and B is a set of bias vectors $\mathbf{b}_i$, $B = \{\mathbf{b}_1, \mathbf{b}_2, \ldots \mathbf{b}_{H+1}\}$ (H is the total number of hidden layers of the MLP network). Accordingly, part of the neural model for the MLP_F and MLP_S networks can be described as:

$$[f_r] = y([R \quad k]^T, W, B) \quad (4)$$

$$[S_{11min}] = y([R \quad k]^T, W, B) \quad (5)$$

respectively. Output of MLP l-th hidden layer, $\mathbf{y}_l$, is represented by the following function:

$$\mathbf{y}_l = F(\mathbf{w}_l \mathbf{y}_{l-1} + \mathbf{b}_l) \quad l = 1,2, \ldots H \tag{6}$$

where $\mathbf{y}_{l-1}$ vector represents the output of (l-1)-th hidden layer, the output of the input layer is a vector $\mathbf{y}_0 = \mathbf{x}$, $\mathbf{w}_l$ is a connection weight matrix among (l-1)-th and l-th hidden layer neurons and $\mathbf{b}_l$ is the vector containing biases of l-th hidden layer neurons. Hyperbolic tangent sigmoid transfer function:

$$F(u) = \frac{e^u - e^{-u}}{e^u + e^{-u}} \tag{7}$$

is used as an activation function of neurons in hidden layers. Activation function of neuron in the output layer is linear so that the output of MLP network is:

$$\mathbf{y} = \mathbf{w}_{H+1} \mathbf{y}_H + \mathbf{b}_{H+1} \tag{8}$$

where $\mathbf{w}_{H+1}$ is the connection weighing matrix between neurons of H-th hidden layer and neurons of output layer and $\mathbf{b}_{H+1}$ is the vector containing biases of output layer.

The notation for such defined MLP neural model, that will be used further in the paper, is MLPH-N_1-…-N_i-…-N_H. N_i represents the number of neurons in the i-th hidden layer. Each network was trained three times with new initial connection weights and thresholds, whose values are random numbers in the interval [-1 1], in order to obtain the best trained model. For example, the notation MLP2-22-15 is used for the MLP model whose neural network has a total of 4 layers (input, output and two hidden layers), this model has 22 neurons in the first and 15 neurons in the second hidden layer.

Neural model was implemented in the MATLAB software environment [16]. For MPL training and testing we generated training and test sample sets by using the EM model of the circular loop antenna described in section II. This data sets have the following format $\{(\mathbf{x}^t, \mathbf{y}^t)\}$, or format $\{([R^t\ k^t], [f_r^t\ \ S_{11min}^t])\}$ where $\mathbf{x}^t$ is the vector of input combinations of the variables R^t and k^t, while $\mathbf{y}^t$ is vector that contains desired outputs of the neural network f_r^t and S_{11min}^t for given input. The notation t in the superscript means that the samples are belonging to training and testing set. The range of input parameters for which the network is trained is $R\,[m] \in [0.020 - 0.100]$ and $k \in [10 - 100]$. This range of input parameters provides achieving resonant frequency for which holds $f_r^t = [500 - 2800]\,[MHz]$, that means that the output band of the model belongs to UHF band as defined according International Telecommunication Union (ITU).

By using the EM model of the planar circular loop antenna and uniform distribution of samples, the following sets for training and testing were generated:

$$\left\{([R^t\ k^t]^T, [\,f_r^t,\ S_{11\min}^t\,]) \,|\, R^t \in [0.02 : d_1 : 0.100], k^t \in [10 : d_2 : 100]\right\} \tag{9}$$

where parameters d_1 and d_2 represent steps and their values d_1 = 0.005 m and d_2 = 2 were used to generate the training set, the values d_1 = 0.007 m and d_2 = 3 were used for the test set. As a result, the training and test sets with 782 and 372 samples, respectively, were obtained. Levenberg-Marquardt training method [7] was used during the model training. Since there are two MLP networks (MLP_F and MLP_S), the appropriate columns from the test and training files are used for each of the networks. In order to obtain the best possible model, the training of a number of MLP neural networks with two hidden layers and different number of neurons in them, was performed. In this process, training and test sets were preprocessed by normalizing the inputs and targets so that they were in the interval [-1,1]. During the training, the target value of the mean square error of the model outputs on the training set was 10^{-4}. During the testing of both networks, three test metrics were observed: values of the worst case error (WCE), values of average test error (ATE) and correlation coefficient [7] for both network outputs, $r^{PPM}(f_r)$ and $r^{PPM}(S_{11\min})$. The goal was to find a neural network with good generalization properties. The testing results for the six MLP_F neural networks with the best test statistics are shown in Table I.

TABLE I
TESTING RESULTS FOR SIX MLP_F NETWORKS WITH THE BEST TEST STATISTICS

MLP_F	WCE[%]	ATE[%]	$r^{PPM}(f_r)$
MLP2-20-15	0.4702	0.1043	0.99999003
MLP2-12-8	0.5881	0.1399	0.99998983
MLP2-17-9	1.1560	0.1775	0.99998961
MLP2-9-6	0.7387	0.1962	0.99998829
MLP2-9-5	0.6632	0.1334	0.99998768
MLP2-10-8	1.1873	0.2896	0.99998756

For the MLP_F part of the neural model, the neural network MLP2-20-15 was chosen, which has the highest value of the correlation coefficient and the lowest value of the worst case error (WCE). The scattering diagram of the MLP2-20-15 neural network on the test set for the output f_r is shown in Fig. 4. The output of the neural model f_r has a very little scatter in relation to the reference values.

The testing results for the six MLP_S neural networks with the best test statistics are shown in Table II.

TABLE II
TESTING RESULTS FOR SIX MLP_S NETWORKS WITH THE BEST TEST STATISTICS

MLP_S	WCE[%]	ATE[%]	$r^{PPM}(S_{11\min})$
MLP2-5-5	26.6089	2.8374	0.9759
MLP2-6-6	28.1494	2.8188	0.9754
MLP2-9-6	25.4494	2.8850	0.9734
MLP2-8-8	26.3811	2.9488	0.9731
MLP2-10-10	24.0547	2.9181	0.9730
MLP2-10-4	30.1837	2.8648	0.9715

For the MLP_S part of the neural model, the neural network MLP2-5-5 was chosen, which has the highest value of the correlation coefficient. The scattering diagram of the MLP2-5-5 neural network on the test set for the output S_{11min} is shown in Fig. 5.

In Fig.5 it can be seen that for $S_{11min} \geq$ -20 dB the scattering for this output of the model is small to moderate. For $S_{11min} <$ -20 dB the scattering is more pronounced which is expected due to the presence of sharp deep peak change in S_{11} values around the resonant frequency.

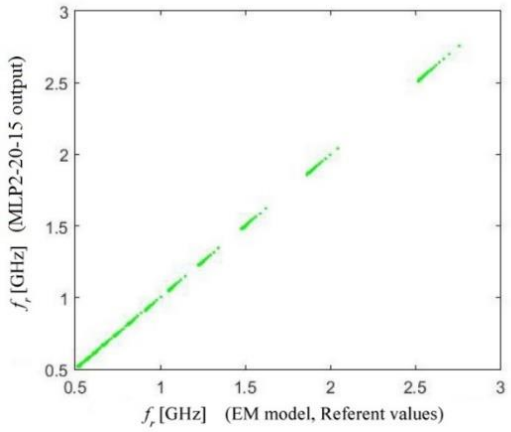

Fig. 4. Scattering diagram of MLP2-20-15 neural model on the test set for f_r output

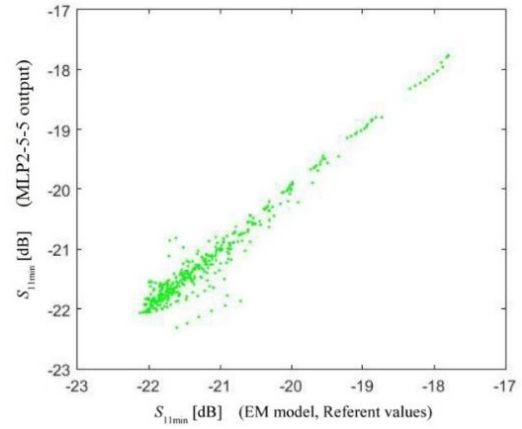

Fig. 5. Scattering diagrams of MLP2-5-5 neural model on the test set for S_{11min} output

However, in that case antenna is already well matched so the reduced model accuracy will not significantly limit its use for an analysis of antenna frequency characteristics such as determining the boundaries and bandwidth of antenna operating frequency range.

Time required to the proposed neural model to simulate 372 points of the test set was 0.04 seconds, while for the same number of points the EM model performed the simulation in 3.23 seconds. Both simulations were performed on a platform whose processor is Intel Core i7 and RAM 12 GB.

IV. Conclusion

Using neural models of planar circular loop antenna, results can be obtained faster and in a simpler way by avoiding complex calculations of Maxwell's equations that take a very long time. The proposed neural model has shown satisfactory accuracy which is very close to the accuracy of EM simulator. Further development will be focused on the optimization of this model, in order to provide the possibility of quickly finding the input parameters for the desired output quantities.

V. Acknowledgment

This work was supported by the Ministry of Education, Science and Technological Development of Republic of Serbia (Grant No. 451-03-9/2021-14/200102).

References

[1] Balanis, C. A., *Antenna Theory: Analysis and Design*, Wiley, New York, 2005.
[2] R. Waterhouse, *Printed Antennas for Wireless Communications*, John Wiley & Sons, Ltd, 2007.
[3] Matthew N. O. Sadiku, *Numerical techniques in electromagnetics*, 2nd edition, CRC Press LLC, 2001.
[4] Levent Sevgi, *Electromagnetic Modeling and Simulation*, First Edition. The Institute of Electrical and Electronics Engineers, Inc. Published by John Wiley & Sons, Inc., 2014
[5] J. Joković, T. Dimitrijević, N. Dončov, "Efficient Modeling of a Circular Patch-Ring Antenna Using the Cylindrical TLM Approach", *IEEE Antennas and Wireless Propagation Letters*, Vol. 16, No. 4, pp. 2070-2073, 2017.
[6] S. Haykin, *Neural Networks*, New York, IEEE, 1994.
[7] Q. J. Zhang, K. C. Gupta, *Neural networks for RF and microwave design*, Boston, MA: Artech House, 2000.
[8] M. Milijić, Z. Stanković and B. Milovanović, "Efficient model of slotted patch antenna based on neural networks,"*2009 9th International Conference on Telecommunication in Modern Satellite, Cable, and Broadcasting Services*, Nis, 2009, pp. 384-387.
[9] M. Pandit, T. Bose, "Application of Neural Network Model for designing Circular Monopole Antenna", *International Symposium on Devices MEMS, Intelligent Systems & Communication (ISDMISC) - Proceedings published by International Journal of Computer Applications (IJCA)*, April 2011, Gangtok, Sikkim, India, pp. 18 -21.
[10] M. Chetioui, A. Boudkhil, N. Benabdallah and N. Benahmed, "Design and optimization of SIW patch antenna for Ku band applications using ANN algorithms,"*2018 4th International Conference on Optimization and Applications (ICOA)*, Mohammedia, 2018, pp. 1-4. DOI: 10.1109/ICOA.2018.8370530.
[11] U. Ozkayaa, L. Seyfia, "Dimension Optimization of Microstrip Patch Antenna in X/Ku Band via Artificial Neural Network", *Procedia - Social and Behavioral Sciences* 195 (2015), pp. 2520 – 2526.
[12] R. Ghayoula, A. Gharsallah, N. Fadlallah and M. Rammal, "Artificial Neural Networks ANN Approach for the Synthesis of Patch Antennas,"*2007 IEEE Radar Conference*, Boston, MA, 2007, pp. 285-290. DOI: 10.1109/RADAR.2007.374229
[13] M. Sarevska, Z. Stankovic, N. Doncov, I. Milovanovic and B. Milovanovic, "Design of well-matched UHF Planar Bowtie Dipole Antenna using Neural Model," 2019 14th International Conference on Advanced Technologies, Systems and Services in Telecommunications (TELSIKS), Nis, Serbia, 2019, pp. 331-334, doi: 10.1109/TELSIKS46999.2019.9002319.
[14] Z. Stankovic, N. Doncov, B.Stosic, M. Sarevska and I. Milovanovic, "Design of well-matched Microwave Slot Antenna on a Flat Metal Grounded Plate using Neural Model", 2020 Information, Communication and Energy Systems and Technologies (ICEST)
[15] https://www.atlasrfidstore.com/what-is-rtls-an-introduction-to-real-time-location-systems/
[16] https://www.mathworks.com
[17] http://ece.wpi.edu/mom/

Modelling of Conformal Antennas using Time-Domain TLM Method

Tijana Dimitrijevic, *Member, IEEE*, Ekrem Altinozen, *Student Member, IEEE*, Aleksandar Atanaskovic, *Member, IEEE*, Jugoslav Jokovic, *Member, IEEE*, Ana Vukovic, *Member, IEEE*, Phillip Sewell, *Senior Member, IEEE*, and Nebojsa Doncov, *Member, IEEE*

***Abstract*—As textile antennas are seeing a major growth in recent years, there is a demand for understanding how they behave when exposed to a realistic environment. Typically, that is done by analyzing the effect of bending on antenna performance. To achieve that, an appropriate, accurate and reliable modeling approach is required. This paper uses two computational methods that employ different discretisation approaches to analyse the effect of bending on antenna performance, namely antenna reflection coefficient. The paper further aims to investigate how the discretisation approach influences the nature and the accuracy of results.**

***Index Terms*—Bending effect, textile antennas, patch antennas, TLM method.**

I. Introduction

WEARABLE applications have experienced an enormous rise in a recent decade fueled by rapid development of 5G technology and continued demand for better health and wellbeing. One of the current challenges in designing wearable antennas is to account for realistic environment which may include the effect of the human tissue but also the impact of arbitrary deformations of textile antenna caused by human movement in everyday activities. Some initial results on the impact of human tissue have been reported in [1-3], showing that the level of performance degradation is dependent on the antenna design.

For the case of arbitrary antenna deformation, a focus has been placed on the special case of cylindrical bending which is also the simplest way of deformation. An analytical model of the cylindrical bending using the cavity mode theory has been presented in [4] with the conclusion that conformally mounted patch antenna that has substrate thickness less than one tenth of the bending radius experiences less than 5% change in resonant frequency and can be therefore treated as a planar antenna [4]. A number of papers used either experimental or simulation approaches to evaluate impact of bending on antenna performance [5-10] and show that bending of antenna can affect the resonant frequency of the antenna. Antenna can be bent along the length of the patch (E-plane) or along the width of the patch (H-plane). Results have shown that E-plane bending has a more significant impact on antenna performance as it directly affects the length of antenna which in turn determines the resonant frequency [7-8]. More recently it has been shown that the thickness of the substrate also plays an important role on how antenna will experience the bending deformation [10].

Whilst experimental measurements are necessary for full deployment, the electromagnetic (EM) computer analysis and simulation plays a vital role in the overall design process. It is important to note that the case of cylindrical bending is the one that can be described using Boolean geometry and as such can be analyzed using commercial time domain EM software that typically uses cubic grid for discretization of the problem space. However, the geometry of the cylindrically bent antenna does not conform to cubic mesh and in order to develop an accurate numerical model the antenna geometry needs to be sampled using a very fine mesh which in turn can demand large computation resources. For example, for time domain computational methods, very fine cubic mesh results in a very small timestep and long runtime. On the other hand, discretization mesh such as cylindrical or tetrahedral mesh that conforms to the structure is preferred as it eliminates the discretization errors and results in much faster and more accurate simulations.

In this paper, the well-established, time domain numerical TLM method has been used to analyze the impact of the bending on textile patch antenna on the S_{11} parameter. The paper considers only the case of E-plane bending as it has a more severe impact on antenna performance. The paper compares the antenna results for several bending angles obtained using TLM method based on the rectangular mesh (recTLM) [11], and the TLM method based on purely cylindrical mesh (cylTLM) [11]. Computational requirements needed for converged results are also compared between these two methods. The paper also seeks to understand whether the type of the mesh used would influence the nature of results. In the following sections a brief description of the TLM method is given, followed by the results and conclusion section.

Tijana Dimitrijevic, Aleksandar Atanaskovic, Jugoslav Jokovic and Nebojsa Doncov are with the Faculty of Electrical Engineering, University of Niš, Aleksandra Medvedeva 14, 18000 Niš, Serbia (e-mail: tijana.dimitrijevic@elfak.ni.ac.rs, aleksandar.atanaskovic@elfak.ni.ac.rs, jugoslav.jokovic@elfak.ni.ac.rs, nebojsa.doncov@elfak.ni.ac.rs).

Ekrem Altinozen, Ana Vukovic and Phillip Sewell are with the Faculty of Engineering, University of Nottingham, Nottingham, UK, (e-mail: ekrem.altinozen1@nottingham.ac.uk, ana.vukovic@nottingham.ac.uk, phillip.sewell@nottingham.ac.uk).

II. The TLM Methodology

The TLM method is a time-domain numerical modeling technique based on equivalences between Maxwell's equations and equations for voltage and current pulses propagation along transmission lines to determine electromagnetic field components [11]. It uses a network of interconnected nodes filling out the propagation space while appropriately representing electromagnetic properties of the homogeneous or inhomogeneous media. A basic TLM cell is the symmetrical condensed node (SCN), but usually HSN (hybrid SCN) node is used to enable modelling of a non-uniform mesh [11]. Depending on the modeling problem, nodes can be generated as cubes or cuboids for Cartesian mesh, "slice of cake" type node for a cylindrical mesh [11] or tetrahedral nodes for an unstructured mesh [12]. Different types of nodes, a cuboid in a Cartesian grid, a part of a slice of cake in a cylindrical grid, and a tetrahedral one, are illustrated in Fig.1.

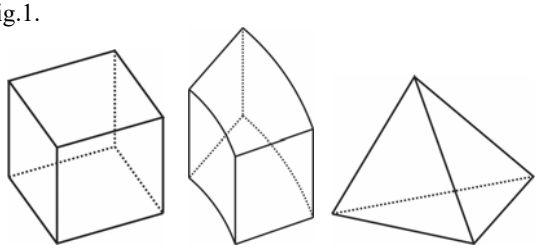

Fig. 1. TLM cell: a) rectangular, b) cylindrical, c) tetrahedral.

In the conventional TLM algorithm, in both rectangular and cylindrical grid, a problem geometry and initial conditions are firstly defined, followed by the calculation of equivalent voltages and currents for each cell, which may be further used to calculate the desired electromagnetic field component. The main algorithm consists of two basic processes that are iteratively repeated for all the nodes within the computational area, and these are, scattering, where reflected voltages at each node are calculated from the incident voltages, and connection where reflected pulses become incident pulses to the neighboring nodes for the next time step. The simulation starts by defining excitation voltages which then propagate through series of reflections and scattering between adjacent nodes while different propagation conditions pertaining to pulse velocity and boundaries are considered. Hence, a dielectric presence is characterized by its relative permittivity and loss tangent. As an output of the simulation, a voltage or a current induced in the wire can be obtained which is further manipulated to determine the reflection coefficient [13].

III. Results and Discussion

The textile patch antenna bent over a cylinder is schematically shown in Fig.2. The patch has the length l and the width w and is bent over the cylinder of radius R over angle 2θ. A coaxial feed is modelled as a wire which is used as an excitation. For the patch antenna considered in this paper, both the patch and the ground plane are described as PEC layers, while the wire is modelled using the compact wire model adapted to the cylindrical mesh [14]. The length and the width of the patch are $l = 50$ mm and $w = 39.5$ mm, respectively, while the length and the width of the substrate and ground plane are $W = L = 100$ mm. It is realized on the substrate of the relative permittivity 2.1 and the thickness $h = 2$ mm. A coaxial feed is placed at 11.5 mm from the patch edge. The flat antenna is designed to resonate at 2.45 GHz.

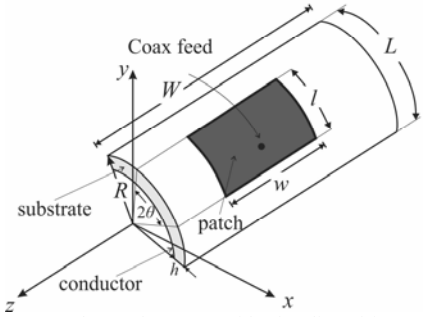

Fig.2. A rectangular patch antenna with a bending 2θ in an E-plane.

To investigate an influence of a curvature on the antenna performances several models of the antenna are considered, and each model is generated for a specific bending angle whilst preserving patch dimensions. All models are meshed with the rectangular and cylindrical TLM mesh. A convergence analysis has been conducted for both recTLM and cylTLM to determine the most adequate mesh. The convergence analysis of the recTLM method is done for the bent antenna with $2\theta = 25$ degrees and for cylindrical case the convergence analysis is done for the case of flat antenna. In both cases the methods consider the structures that do not conform to a particular mesh type. In the case of cylTLM, the flat antenna has been designed by applying very small bending angle, i.e., $2\theta = 0.1$ degrees (corresponding to the radius of $R = 22.63$ m in a cylindrical grid), i.e. $R >> l$, hence it can be considered as the flat one. Fig.3 shows the convergence of the resonant frequency for different mesh size Δl, where Δl represents the cell size within an area around the structure with a refined mesh applied. In the cylTLM method, this area is simply the substrate area.

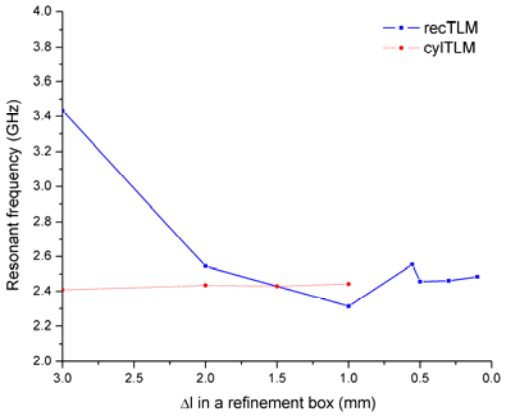

Fig.3. Illustration of the resonant frequency convergence with the mesh refinement when the recTLM method (blue line) is used for the bent antenna, and cylTLM method (red line) is used for the flat antenna (Δl represents the observed cell size).

As can be seen, the resonant frequency of the antenna converges to a different value in the recTLM and cylTLM method. This is as expected since the bending affects the resonant frequency. Furthermore, the recTLM achieves convergence for much smaller values of Δl confirming that discretization error around the curved surfaces can affect the convergence analysis. The cylTLM on the other hand has much smoother and faster convergence since the mesh is ideally suited to the structure even though the considered antenna is almost flat resulting in 10 times smaller mesh for the converged result compared to recTLM.

The comparison of a number of cells and their dimensions required for different mesh types is shown in Table 1. It shows that rectangular TLM requires much larger computational resources than cylindrical TLM, resulting in about 6 times larger mesh when 0.5 mm rectangular cell size is used, and about 360 times larger mesh for 0.1 mm cell size. This is a significant advantage of cylindrical TLM method for this particular application.

Table 1. The comparison of computational mesh size between recTLM and cylTLM approach

Method	Cell size (general mesh/ refined area)	Number of nodes	Wire radius
recTLM	1 mm/0.5 mm	80×280×260 ~6M	0.1mm
recTLM	1 mm/0.1 mm	240×1240×1140 339M	0.025mm
cylTLM	1.449 mm/1 mm	151×42×149 944k	0.1mm

For the case of flat antenna, the cylTLM method with 1 mm mesh gives resonant frequency at 2.443 GHz and the recTLM gives resonant frequency at 2.454 GHz if 0.5 mm mesh is used and 2.492 GHz if 0.1 mm mesh is used. Further investigation has included modeling of antennas cases with a different bending angle, i.e., 2θ=25, 50 and 60 degrees, while patch dimensions are kept the same. The S_{11} results obtained using cylTLM, and recTLM methods are shown in Figs. 4 and 5, respectively. The S_{11} of the flat antenna is also included in figures for reference. All results show that resonant frequency values are influenced by the curvature. According to the Fig.4, when the cylTLM approach is used, results show that the resonant frequency is increased with rising the bending angle in an almost linear fashion, while the matching condition is affected as well. However, in the case of recTLM method, as presented in Fig.5a, the trend is different for coarser mesh (0.5 mm), showing reduction in resonant frequency for various bending angles compared to Fig.4. When a finer mesh is used (0.1mm), as shown in Fig.5b the trend is more similar to the cylTLM results. A difference between the resonant frequency values by two approaches might be attributed to introducing the wire for excitation of much smaller wire radius in the recTLM than in the cylTLM approach, due to a much smaller cell size. Also, a better matching is possible to achieve when a finer rectangular mesh is used.

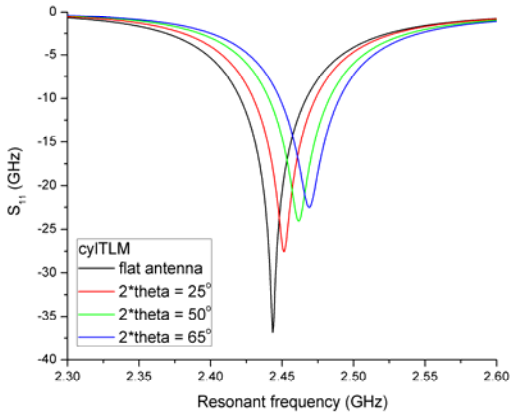

Fig.4. Comparison of S11 parameter of the flat antenna and antenna bent over a cylinder of angle 2θ =25, 50 and 60 degrees. Results are obtained using cylTLM method (1.0 mm cell size).

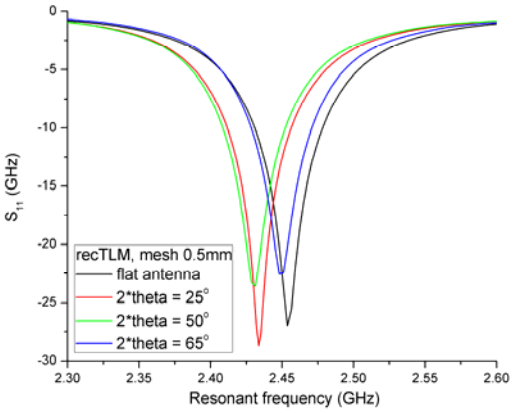

a)

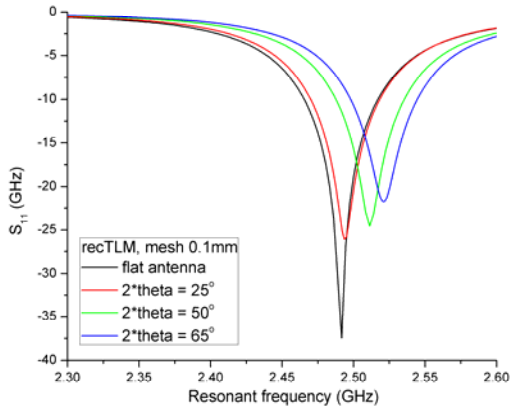

b)

Fig.5. Comparison of S11 parameter of the flat antenna and antenna bent over a cylinder of angle 2θ =25, 50 and 60 degrees. Results are obtained using recTLM method with a) courser mesh (0.5 mm cell size), b) finer mesh (0.1 mm cell size).

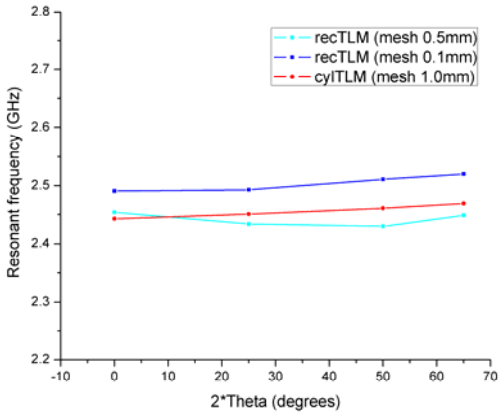

Fig.6. The resonant frequency vs the bending angle (2*theta) of the flat and bent rectangular patch antenna obtained by recTLM, and cylTLM approaches.

Fig. 6. presents the comparison of the resonant frequency reached via these two methods for various bending angles. Fig.7. reveals that the maximum frequency shift when the cylTLM approach is applied is 26 MHz, while the recTLM approach with the courser mesh gives 13 MHz, and 29 MHz for the finer mesh.

According to the presented results and the ease of convergence of the cylTLM method it can be concluded that results obtained using cylTLM method agree much better with the reported literature stating that E-plane bending causes the resonant frequency to shift to higher frequencies. The results obtained using the recTLM method are heavily affected by the discretization error which is confirmed by comparing results obtained using 0.5 mm and 0.1 mm mesh. It can be concluded that only a very fine mesh is needed so that the discretization error is not affecting the main EM phenomena.

IV. Conclusion

In this paper, the well-established TLM method is applied to investigate the influence of the curvature on the rectangular patch antenna resonant frequency. Two different types of the TLM mesh, based on different cell geometries are used, namely the rectangular, and the cylindrical TLM method. Results show that when using rectangular TLM method a very fine mesh must be used to minimize the discretization error and observe correct behavior. This is not the case for the cylTLM method as the mesh is perfectly aligned with the structure resulting in a tenfold increase in the mesh size and significant reduction in computation time and memory. The converged results of both methods show that when antenna is bent in the E-plane the resonant frequency of antenna shifts to higher frequencies.

Acknowledgment

This work was supported by the Ministry of Education, Science and Technological Development of Republic of Serbia (Grant No. 451-03-9/2021-14/200102), Science Fund of the Republic of Serbia (Grant No. 6394135), and the Royal Society International Exchanges Grant IES\R1\201311.

References

[1] J. S. Colburn and Y. Rahmat-Samii, "Human proximity effects on circular polarized handset antennas in personal satellite communications," in *IEEE Transactions on Antennas and Propagation*, vol. 46, no. 6, pp. 813-820, June 1998, doi: 10.1109/8.686767.

[2] S. S. Zhekov and G. F. Pedersen, "Effect of Dielectric Properties of Human Hand Tissue on Mobile Terminal Antenna Performance," *2020 14th European Conference on Antennas and Propagation (EuCAP)*, 2020, pp. 1-5, doi: 10.23919/EuCAP48036.2020.9135910.

[3] M. Koohestani, N. Pires, A. K. Skrivervik and A. A. Moreira, "Performance Study of a UWB Antenna in Proximity to a Human Arm," in *IEEE Antennas and Wireless Propagation Letters*, vol. 12, pp. 555-558, 2013, doi: 10.1109/LAWP.2013.2259212.

[4] C. Krowne, "Cylindrical-Rectangular Microstrip Antenna. Antennas and Propagation," *IEEE Transactions on. AP*-31, 194 – 199, 1983.

[5] I. Locher, M. Klemm, T. Kirstein and G. Troster, "Design and Characterization of Purely Textile Patch Antennas," in *IEEE Transactions on Advanced Packaging*, vol. 29, no. 4, pp. 777-788, Nov. 2006, doi: 10.1109/TADVP.2006.884780.

[6] C. Hertleer, A. Tronquo, H. Rogier, L. Vallozzi and L. Van Langenhove, "Aperture-Coupled Patch Antenna for Integration Into Wearable Textile Systems," in *IEEE Antennas and Wireless Propagation Letters*, vol. 6, pp. 392-395, 2007, doi: 10.1109/LAWP.2007.903498.

[7] M. Tanaka and Jae-Hyeuk Jang, "Wearable microstrip antenna," *IEEE Antennas and Propagation Society International Symposium. Digest. Held in conjunction with: USNC/CNC/URSI North American Radio Sci. Meeting (Cat. No.03CH37450)*, 2003, pp. 704-707 vol.2, doi: 10.1109/APS.2003.1219333.

[8] F. Boeykens, L. Vallozzi, H. Rogier, "Cylindrical Bending of Deformable Textile Rectangular Patch Antennas", *International Journal of Antennas and Propagation*, vol. 2012, Article ID 170420, 11 pages, 2012.

[9] M. E. Bakkali, M. Martinez-Estrada, R. Fernandez-Garcia, I. Gil and O. E. Mrabet, "Effect of Bending on a Textile UHF-RFID Tag Antenna," *2020 14th European Conference on Antennas and Propagation (EuCAP)*, 2020, pp. 1-5, doi: 10.23919/EuCAP48036.2020.9135331

[10] L. Song and Y. Rahmat-Samii, "A Systematic Investigation of Rectangular Patch Antenna Bending Effects for Wearable Applications," in *IEEE Transactions on Antennas and Propagation*, vol. 66, no. 5, pp. 2219-2228, May 2018, doi: 10.1109/TAP.2018.2809469.

[11] C. Christopoulos, The Transmission-Line Modeling Method: TLM. New York, NY, USA: Wiley, 1995.

[12] P. Sewell, T. M. Benson, C. Christopoulos, D. W. P. Thomas, A. Vukovic and J. G. Wykes, "Transmission-line modeling (TLM) based upon unstructured tetrahedral meshes," in *IEEE Transactions on Microwave Theory and Techniques*, vol. 53, no. 6, pp. 1919-1928, June 2005, doi: 10.1109/TMTT.2005.848078.

[13] T. Z. Dimitrijevic, J. J. Jokovic and N. S. Doncov, "Efficient Modeling of a Circular Patch-Ring Antenna Using the Cylindrical TLM Approach," in *IEEE Antennas and Wireless Propagation Letters*, vol. 16, pp. 2070-2073, 2017, doi: 10.1109/LAWP.2017.2696122.

[14] T. Ž. Dimitrijević, J. J. Joković, B. D. Milovanović, N. S. Dončov, "TLM Modelling of a Probe-coupled Cylindrical Cavity based on Compact Wire Model in the Cylindrical Mesh", International Journal of RF and Microwave Computer-Aided Engineering, John Wiley & Sons Inc., Wiley InterScience Periodicals, Vol.22, No. 2, pp. 184-192, 2012. DOI: 10.1002/mmce.20569

Reduced Dimensions Planar Rat Race Coupler Design

Denis A. Letavin and Dusan A. Nesic, *Member, IEEE*

***Abstract*—The design of a rat race directional coupler was investigated in the Cadence AWR Design Environment program. By using low-pass filters instead of quarter-wave sections, it was possible to reduce the size of the device by 82.3%. In this case, the following deterioration of frequency characteristics occurred: narrowing of the operating frequency band by 19.3%, an increase in imbalance, and a decrease in matching. Also, the area of the compact double ring coupler was reduced by 84.5% while the bandwidth was narrowed by 29.2%.**

***Index Terms*—Filter, miniaturization, stub, coupler.**

I. Introduction

THE rat race directional coupler functions as a signal power divider with two phase differences, 0 and 180 degrees, depending on which port is considered to be the input port. The topology of such a device consists of four segments, three of which have an electrical length of 90 degrees, and the remaining 270 degrees. After combining such segments, a ring with a length of 1.5 wavelengths per line is obtained. Due to the fact that the wavelength and frequency are related, the lower the operating frequency of the device, the more area on the printed circuit board it will have. Therefore, at low frequencies, where the couplers turn out to be cumbersome, its miniaturization is actual, with the minimum possible deterioration of frequency characteristics. There are a lot of options for miniaturizing the spokesmen. Let's take a look at just a few. The following approaches are used to miniaturize tap-off devices: microstrip cells [1], T-shaped structures [2], dual-transmission lines [3], using C-SCMRC resonators with distributive equivalent circuit [4], artificial transmission lines [5, 10, 14, 15], resonators [6, 7, 13], circular defected ground structure [8], shunt-stub-based artificial transmission lines [9], multilayer LTCC [11, 12]. In the proposed work, a method is considered for obtaining a compact ring coupler by replacing all quarter-wave sections with low-pass filters. Also considered is a compact double ring coupler, which, due to the addition of one more circuit, increases the operating frequency band and dimensions.

Dusan Nesic is with Centre of Microelectronic Technologies, Institute of Chemistry, Technology and Metallurgy, University of Belgrade, Njegoševa 12, 11000 Belgrade, Serbia (mail: nesicad@nanosys.ihtm.bg.ac.rs)

Denis A. Letavin is with the Institute of Radioelectronics and Informational Technologies, Ural Federal University, Mira str. 32, 620002 Ekaterinburg, Russia (e-mail: d.a.letavin@urfu.ru)

II. Design Coupler

A circular directional coupler is a type of power divider used in microwave technology. Using the Cadence AWR DE program and the built-in TXLine calculator, the topology of a standard coupler was calculated (Fig. 1). The well-known FR4 material acts as a substrate material, with ε = 4.4 and h = 1 mm, and as a central frequency of 1 GHz. The obtained frequency characteristics of the coupler in the AWR program are illustrated in Figures 2 and 3. The area of the device is 43 x 91.5 = 3934.5 mm^2.

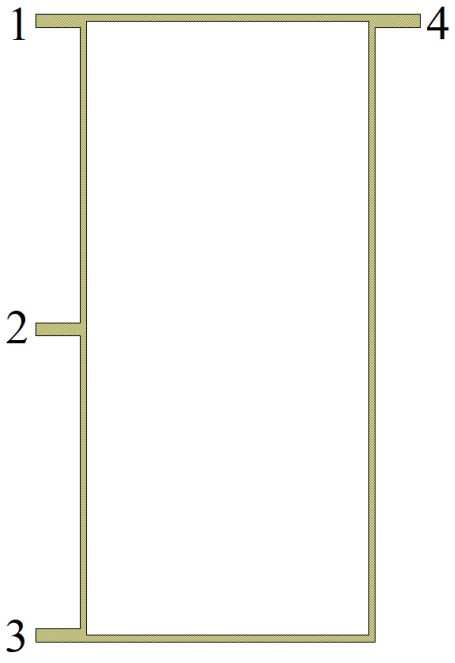

Fig. 1. Standard rat race coupler layout

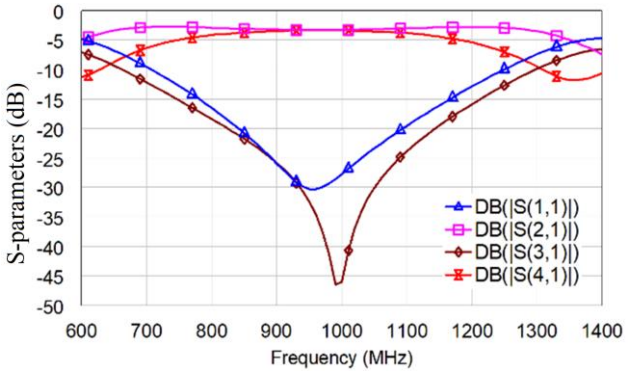

Fig. 2. S-parameter versus frequency plot for a standard rat race coupler

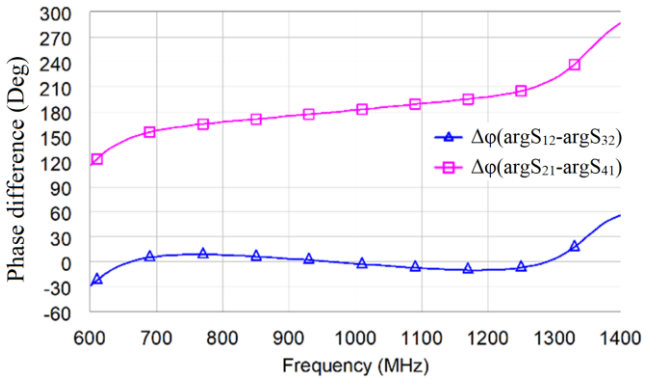

Fig. 3. The graph of the phase difference of the output signals depending on the choice of the input port (blue line - 1 input port, pink line - 4 input port)

According to the graphs obtained, it can be seen that the operating frequency band of the coupler at the isolation level "minus" 20 dB is 320 MHz (824-1144 MHz). The imbalance between the output signals of the structure in the frequency band does not exceed 1.3 dB. The area inside the coupler is not used in any way, which is an additional disadvantage of such a device. To reduce the size of the ring coupler, the required low-pass filters are initially calculated, which are used instead of the quarter-wave sections. For this purpose, a filter is calculated for the required wave impedance of 70.7 Ohm, which has a phase incursion of 90 degrees at a central frequency of 1 GHz. Filters can be implemented in a T-shaped or U-shaped circuit (Figure 4). They are completely equivalent to each other and can be used with equal efficiency. However, in our case, a U-shaped circuit was chosen, due to the fact that the extreme capacitive elements can be combined with the extreme elements from other filters, which can make it possible to more successfully fill the space inside the coupler. Low-pass filters can be calculated using the built-in iFilter tool in the Cadence AWR software.

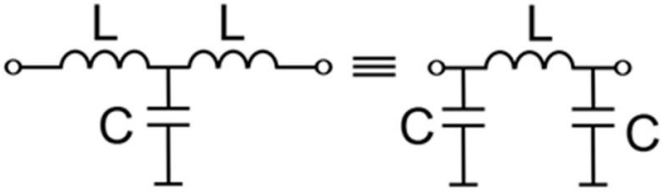

Fig. 4. T-shaped and U-shaped low-pass filter circuit

To calculate the ratings of CLC (capacitance - inductance - capacitance) elements, it is necessary to know the characteristic impedance of the transmission line, the parameters of the substrate material, the central frequency at which it is necessary to provide a phase shift of 90 degrees. After all filters are calculated, they are gradually installed instead of the quarter-wave sections of the coupler. The arrangement of the filter elements is carried out in such a way that there is no electrical contact between the elements of adjacent filters. After this procedure, an electrodynamic design calculation is performed, and if the frequency characteristics are unsatisfactory, then a forced optimization of the coupler design is performed in order to obtain the required characteristics. The topology of the compact ring coupler is shown in Figure 5. The obtained frequency characteristics of the compact coupler in the AWR program are illustrated in Figures 6 and 7.

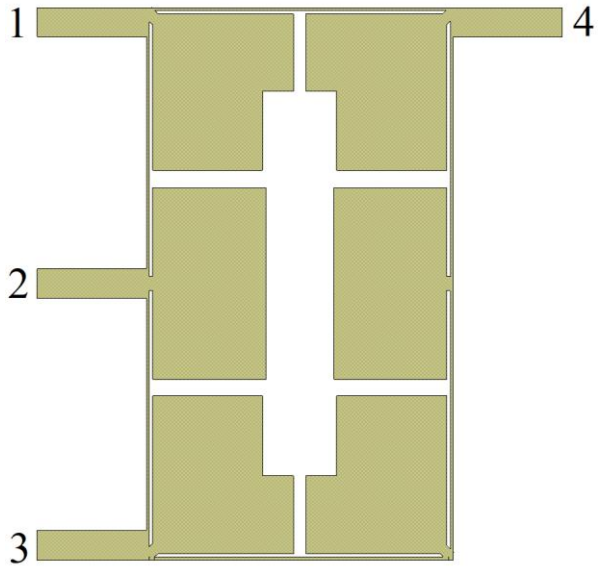

Fig. 5. Compact rat race coupler

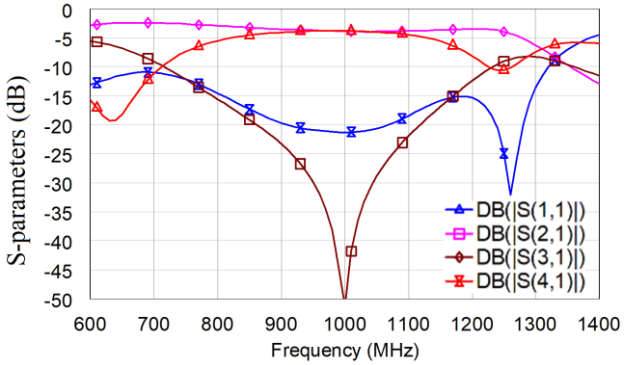

Fig. 6. S-parameter versus frequency plot for a compact rat race coupler

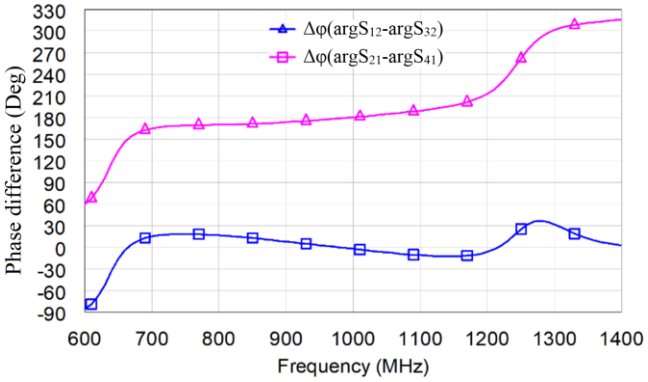

Fig. 7. The graph of the phase difference of the output signals depending on the choice of the input port (blue line - 1 input port, pink line - 4 input port)

By replacing the quarter-wave sections with low-pass filters and using the area inside the device, it was possible to reduce the area of the device by 82.3%. In a miniature version, the coupler has an area equal to 19.65 x 35.5 = 697.6 mm^2. According to the graphs obtained, it can be seen that the operating frequency band of the coupler at the isolation level "minus" 20 dB is 258 MHz (860-1118 MHz). The imbalance

between the output signals of the structure does not exceed 1.1 dB. As a result of the miniaturization of the coupler, the operating frequency band was narrowed by 19.3%. The differences are primarily due to the incomplete coincidence of the characteristics of the quarter-wave sections and the elements installed instead of them. From the data in Table 1, you can compare the characteristics of the standard and miniature coupler.

TABLE I
COMPARATIVE DATA OF COUPLER

Parameters	Standard	Compact
bandwidth, MHz	320	258
Area, mm^2	3934,5	697,6
Relative area, %	100	17.7
Central frequency, MHz	1000	1000
The phase outputs on the central frequency, °	0 180	1.8 180.3

To increase the bandwidth of operating frequencies, an additional circuit is added to the design of the coupler, the length of which is equal to the wavelength in the line. To increase the bandwidth of the quadrature directional couplers, the addition of additional stub lines (cascading) is used. In the case of ring (common-phase-antiphase) taps, cascading is also used to increase the bandwidth. The dual ring coupler topology is shown in Figure 8. A single wavelength loop is added to the coupler design, with a characteristic impedance of 100 ohms. To further increase the strip, a third and subsequent circuit can be added, but this will lead to an increase in dimensions and complicate the design of the device. Low-pass filters are also asymmetrically designed to occupy the internal area of the coupler and further reduce the size of the device. The obtained frequency characteristics of the compact coupler in the AWR program are illustrated in Figures 9 and 10.

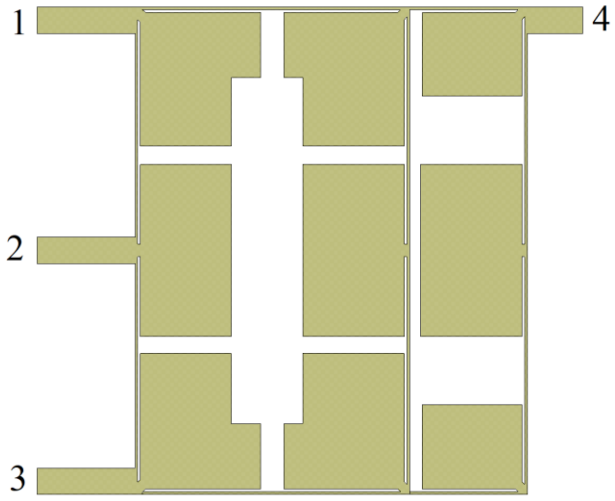

Fig. 8. Compact double rat race coupler

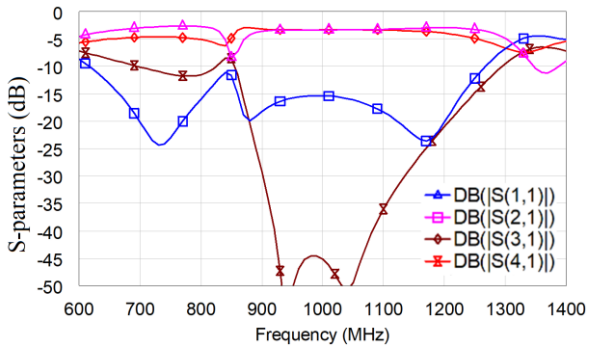

Fig. 9. S-parameter versus frequency plot for a compact double rat race coupler

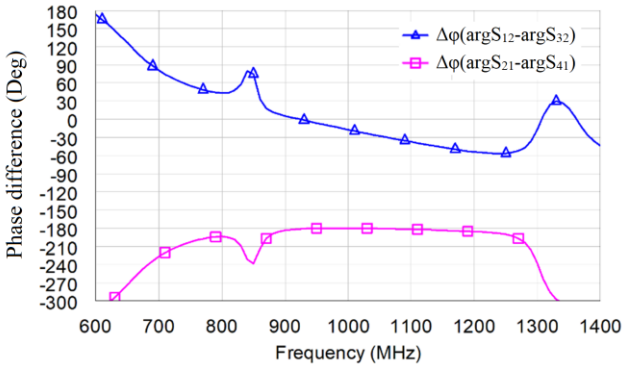

Fig. 10. The graph of the phase difference of the output signals depending on the choice of the input port (blue line - 1 input port, pink line - 4 input port)

By adding a loop, it was possible to increase the operating frequency band of the coupler to 329 MHz. At the same time, the area of the device increased to 977.2 mm^2. From the data in Table 2, you can compare the characteristics of the standard and miniature coupler.

TABLE II
COMPARATIVE DATA OF COUPLER

Parameters	Standard	Compact
bandwidth, MHz	465	329
Area, mm^2	6302	977.2
Relative area, %	100	15.5
Central frequency, MHz	1000	1000
The phase outputs on the central frequency, °	0 180	12 180

III. CONCLUSION

A miniature ring coupler obtained by replacing quarter-wave sections with low-pass filters is investigated in this work. Filter elements are located in the internal space of the device. All this made it possible to reduce the area of the coupler by 82.3% with a relative bandwidth of 25.8%, which is 19.3% less than that of a standard device. A double ring coupler was also obtained, the area of which is 84.5% less than the area of its standard implementation, with a relative bandwidth of 32.9%, which is 29.2% less than that of a standard device.

REFERENCES

[1] Piotr Kurgan and Slawomir Koziel, "EM-driven compact cell topology selection for explicit size reduction of hybrid rat-race couplers," 2017 47th European Microwave Conference (EuMC). DOI: 10.23919/EuMC.2017.8230864.

[2] Vamsi Krishna Velidi, Sarika Shrivastava and Subrata Sanyal, "A compact-size microstrip rat-race coupler with high performance," IEEE Technology Students' Symposium. DOI: 10.1109/TECHSYM.2011.5783801.

[3] Po-Hsiang Tu and Chao-Hsiung Tseng, "Design of a compact rat-race coupler using dual transmission lines," 2010 Asia-Pacific Microwave Conference.

[4] Jianzhong Gu and Xiaowei Sun, "Miniaturization and harmonic suppression rat-race coupler using C-SCMRC resonators with distributive equivalent circuit," IEEE Microwave and Wireless Components Letters. DOI: 10.1109/LMWC.2005.859980.

[5] Slawomir Koziel and Adrian Bekasiewicz, "Novel structure and size-reduction-oriented design of microstrip compact rat-race coupler," 2016 IEEE/ACES International Conference on Wireless Information Technology and Systems (ICWITS) and Applied Computational Electromagnetics (ACES). DOI: 10.1109/ROPACES.2016.7465390.

[6] Tsu-Wei Lin, Jen-Yi Wu and Jen-Tsai Kuo, "Filtering rat-race coupler with transmission zeros using compact miniaturized hairpin resonators," 2015 IEEE International Wireless Symposium (IWS 2015). DOI: 10.1109/IEEE-IWS.2015.7164553.

[7] Zhebin Wang, Jae-Sik Jang and Chan-Wang Park, "Tri-band rat-race coupler using resonators," 2011 IEEE International Conference on Microwave Technology & Computational Electromagnetics. DOI: 10.1109/ICMTCE.2011.5915197.

[8] Saraunsh Bayaskar, Dewang Brahme and K Shambavi, "Compact rat race coupler with harmonic suppression using Circular defected ground structure (CDGS)," 2016 International Conference on Global Trends in Signal Processing, Information Computing and Communication (ICGTSPICC). DOI: 10.1109/ICGTSPICC.2016.7955319.

[9] Chao-Hsiung Tseng and Hsiang-Ju Chen, "Compact Rat-Race Coupler Using Shunt-Stub-Based Artificial Transmission Lines," IEEE Microwave and Wireless Components Letters. DOI: 10.1109/LMWC.2008.2005225.

[10] Letavin Denis A., "Miniature microstrip rat-race couplers with artificial transmission lines," 2017 40th International Conference on Telecommunications and Signal Processing (TSP). DOI: 10.1109/TSP.2017.8076099.

[11] Tze-Min Shen, Chin-Ren Chen, Ting-Yi Huang and Ruey-Beei Wu, "Dual-band rat-race coupler design in multilayer LTCC," 2010 Asia-Pacific Microwave Conference.

[12] Chao-Hsiung Tseng, "Compact LTCC Rat-Race Couplers Using Multilayered Phase-Delay and Phase-Advance T-Equivalent Sections," IEEE Transactions on Advanced Packaging. DOI: 10.1109/TADVP.2010.2044660.

[13] Wei-Hsin Wang, Tze-Min Shen, Ting-Yi Huang and Ruey-Beei Wu, "Miniaturized rat-race coupler with bandpass response and good stopband rejection," 2009 IEEE MTT-S International Microwave Symposium Digest. DOI: 10.1109/MWSYM.2009.5165795.

[14] Gerard Siso, Jordi Bonache, Marta Gil, Joan Garcia-Garcia and Ferran Martin, "Compact Rat-Race Hybrid Coupler Implemented Through Artificial Left Handed and Right Handed Lines," 2007 IEEE/MTT-S International Microwave Symposium. DOI: 10.1109/MWSYM.2007.380209.

[15] Letavin D.A., “Bandwidth miniature quadrature branch line coupler design,” 2020 28th Telecommunications Forum, TELFOR 2020, November 2020. DOI: 10.1109/TELFOR51502.2020.9306606.

Experimental Analysis of Electromagnetic Interferences Absorber Influence on Metal Enclosure Immunity

Nataša J. Nešić, Slavko S. Rupčić, *Member, IEEE,* Vanja Mandrić-Radivojević, *Member, IEEE,* and Nebojša S. Dončov, *Senior Member, IEEE*

***Abstract*—This paper considers the experimentally conducted analysis of shielding effectiveness of an enclosure with electromagnetic interferences absorber placed at different positions inside. Dimensions of an absorber sheet are fitted to affect the enclosure's first resonant frequency in order to improve its protective function. An absorber sheet inside measured enclosure has an impact on the shielding effectiveness values not only at the first resonance but also in a wider frequency range.**

***Index Terms*—Absorber, Enclosure, EMI absorber sheet, Measurements, Shielding Effectiveness.**

I. Introduction

A common technique to protect electronic equipment from an external electromagnetic (EM) field and an electromagnetic interference (EMI) as well to limit a level of EM field, caused by equipment itself and radiated to surroundings, is to apply shielding [1]. A shielding enclosure may be constructed using steel, aluminum, copper or any other highly conductive material. Still, there are a number of different multipath coupling mechanisms, such as through apertures and cables, which can reduce a protective function of enclosure, usually expressed as the shielding effectiveness (SE). The SE can be determined as logarithmic ratio of electric field with and without shielding enclosure, in the same probe point. Also, the shielding characteristics of an enclosure can indicate negative values of the SE, especially at resonant frequencies of enclosure. Thus, the useful frequency range, in which EM shielding is provided, might be compromised.

To improve the shielding properties, several techniques can be applied. For instance, in [2] and [3], the SE of enclosure was increased by using absorbers or conductive foam. In [4] and [5], the authors proposed to suppress the first resonance in a metal enclosure by putting small antenna elements with loaded resistance. By placing a small dipole or loop antenna structure on the enclosure wall opposite to the enclosure aperture, it was shown that the EM shielding could be improved. In addition to that, it was numerically demonstrated in [6] and the experimentally confirmed in [7] that the physical dimensions of receiving-antenna, often used in experimental set-up to measure a level of EM field, could also affect the SE of enclosure.

In this paper, an influence of an EMI absorber on the SE of enclosure having the frontal wall with rectangular aperture is experimentally studied. During this study, this thin EMI absorber sheet is placed on one or more inner enclosure walls with the goal to consider how the position of absorber affects the SE behavior at the first resonance of enclosure but also at higher resonances. Some other EMI absorber positions inside the same considered enclosure are discussed in [9]. The paper is organized as follows. Section II refers to a physical enclosure's model with the EMI absorber material and a receiving-antenna inside. In Section III, the experimental set-up and measurement procedure are described. Section IV provides discussion of the experimental results. Finally, Section V summarizes the work.

II. Physical Model of Enclosure

The physical enclosure, which is used in the experimental measurements, with the monopole-receiving antenna and the absorber inside is shown in Fig.1. It has a front wall with rectangular aperture (not shown in Fig.1). The enclosure walls are made from copper material. The thickness of the enclosure walls is t = 1.5 mm. The metal enclosure entitled by D has a rectangular shape, with internal dimensions of (300x300x120) mm^3. On the front wall of the enclosure, a slot of dimensions (100x5) mm^2 is positioned symmetrically around the center on the frontal wall. An in-house monopole antenna is placed in the middle of the enclosure to measure the level of EM field inside. An antenna is made of copper wire with a length of 60 mm and radius of 0.1 mm. In order to prevent EM wave leakage from the tested enclosure, a copper strip is bonded to the joints.

Specifically, the absorber material is thin as a sheet of paper and it does not occupy significant space inside the enclosure. The 3M™ EMI Absorber AB7050 from AB7000 Series was available and therefore, it is used in this paper. One side consists of a flexible polymer resin loaded with soft metal flakes and on the other side is covered by an acrylic pressure-sensitive adhesive allows for easy application. This absorber is typically used for applications requiring EMI control and signal integrity improvement in the 50 MHz to 10

Nataša J. Nešić is with the Department of Information and Communication Technologies at Academy of Applied Technical and Preschool Studies Niš, Aleksandra Medvedeva 20, 18000 Nis, Serbia (e-mail: natasa.nesic@akademijanis.edu.rs).

Slavko M. Rupčić and Vanja Mandrić-Radivojević are with Department of Communications, Faculty of Electrical Engineering, Kneza Trpimira 2b, Osijek 31000, Croatia, (e-mails: rupcic@etfos.hr, vanja.mandric@etfos.hr).

Nebojša S. Dončov is with the Faculty of Electronic Engineering Niš, University of Niš, Aleksandra Medvedeva 14, 18000 Niš, Serbia (e-mail: nebojsa.doncov@elfak.ni.ac.rs).

GHz range. It is a broadband EMI absorber designed to work in near-field applications inside and around electronic devices and assemblies [8]. Many factors determine the true attenuation of an EMI absorbing material, including shape and thickness, intimacy of substrate contact, smoothness of application surface, strength and frequency of the EMI signal, etc. [8].

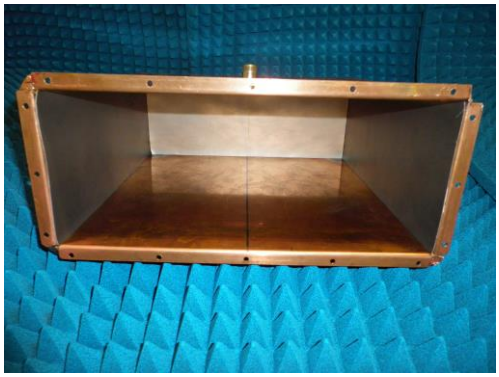

Fig. 1. Physical model of *D* metal enclosure with the EMI absorber on the wall opposite to the frontal enclosure wall and on both side walls.

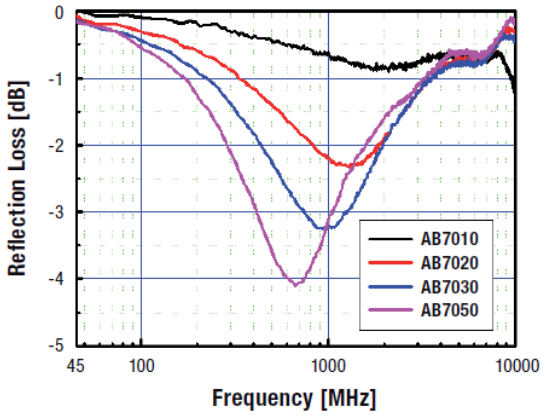

Fig. 2. The reflection loss of the EMI absorber AB7050 sheet which is used for measurement purposes, [8].

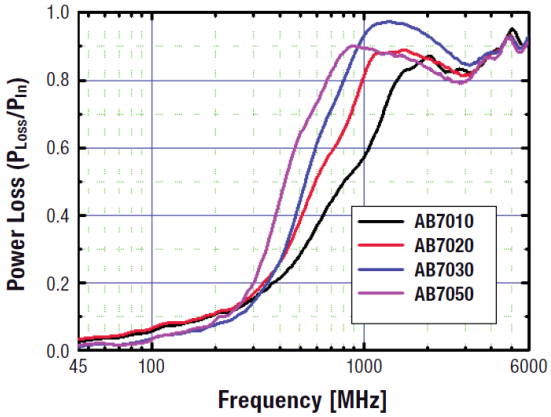

Fig. 3. The power loss of the EMI absorber AB7050 sheet which is used for measurement purposes, [8].

Figs. 2 and 3 present the reflection loss and the power loss of the EMI absorber, respectively, taken from [8]. The absorber characteristics and physical dimensions are given in Table I.

The EMI absorber sheet inside the enclosure *D* is placed in different positions in order to see how it will enhance the shielding characteristics of enclosure especially at the first resonant frequency. Firstly, the absorber is employed on the wall opposite to the front wall with an aperture which is entitled by BcW (back wall). Its dimensions correspond to the internal dimensions of the back enclosure's wall. Secondly, the absorbers are put on both side enclosure walls – entitled by 2SW (two side walls). The dimensions of the absorber are cut to fit the enclosure's side walls which is (297x120) mm^2. In the third case, the absorbers are employed at the same time on all above-mentioned positions, as depicted in Fig. 1. The SE characteristics obtained for this case will be called BcW+2SW.

TABLE I
THE EMI ABSORBER CHARACTERISTICS [8]

Property	Typical Value			
Adhesive	Acrylic non-conductive pressure-sensitive adhesive (PSA)			
Type of backing	Polymer resin with magnetic metal flake filter			
Product number	AB7010	AB7020	AB7030	**AB7050**
Backing thickness	0.1mm	0.2mm	0.3.mm	0.5mm
Adhesive thickness	0.03mm	0.05mm	0.05mm	0.05mm
Standard packaging	210 mm x 297 mm			
Temperature range	-25ºC ~ 85ºC			
Surface Resistivity	1 x 10^6 Ω (min)			
Initial permeability	110			
Typical performance	Refer to S_{11} attenuation and power loss graphs			

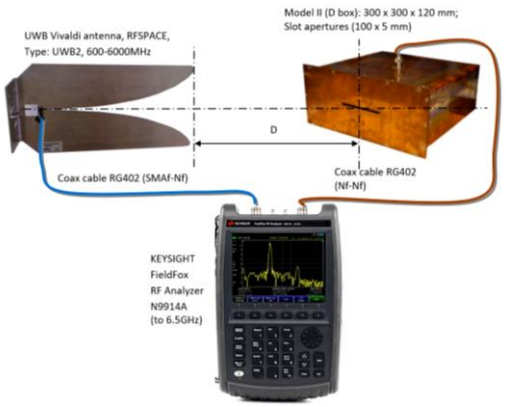

Fig. 4. The sketch of the measuring set-up: transmitting antenna, VNA and EUT (enclosure under test *D*).

III. EXPERIMENTAL PROCEDURE

The measurements are performed in a semi-anechoic room and the measuring set-up is illustrated in Figs. 4 and 5. The Keysight Field Fox RF Analyzer N9914A 6.5 GHz, with a resolution of 100 Hz and a maximum power of 3 dBm, is used as vector network analyzer (VNA). It is connected via cables to a transmitting antenna and a receiving antenna. A vertically polarized dipole antenna of type Vivaldi, as a broadband-antenna with a frequency range from 600 MHz to 6 GHz, is used as a transmitting antenna. As already mentioned, an in-house monopole antenna is used as a receiving antenna. All measurements are taken in the frequency range from 600 MHz to 2 GHz. The measurements are performed in the far-field. The distance is calculated to match that the enclosure under

test (EUT) is in the far-field, which is marked as distance (*D*) in Fig. 4. The EMI absorber used in the experimental analysis is cut to fit the inner enclosure's sides.

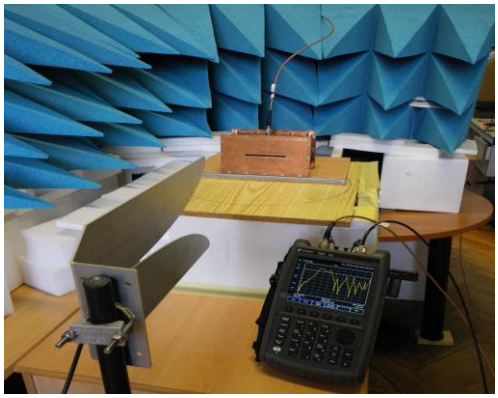

Fig. 5. The measuring configuration used in the semi-anechoic room.

The SE of enclosure is obtained by measure the electric field of EUT with monopole antenna inside and by measure the electric field of monopole antenna without enclosure, in the same probe point (the center of the considered enclosure) [7]. The SE of EUT is obtained by measuring the transmission parameters by using the network analyzer. It is measured twice, without and with enclosure which are marked as s_{21n} and s_{21e}, respectively. Therefore, the SE can be calculated by the following equation: SE [dB] = s_{21n} - s_{21e}.

IV. Discussion of Results

This section presents the experimental results of the SE of enclosure with the EMI absorber inside. To start with, the SE measurement results of enclosure *D* with the absorber employed on the wall opposite to the frontal wall with an aperture, are presented in Fig. 6. The SE results are obtained based on the measured level of EM field inside the enclosure. Figure 6 contains also the SE results for the case of enclosure without absorber (empty enclosure with only receiving antenna inside). As it can be seen from Fig. 6, a physical presence of the absorber led to the SE improvement of enclosure *D* in comparison to the empty enclosure case. In terms of shape, the compared SE curves are similar, however it can be observed that both curves differ regarding the SE levels not only around the first resonance but also at the second resonant frequency. The first resonance of empty enclosure is 686 MHz and the SE value is equal to -14.95 dB, which is critical and might compromise enclosure's shielding properties. On the other hand, the first resonance of enclosure with the EMI absorber occurs at 694 MHz and its SE has a positive value of 5.45 dB. The difference between the SE levels (ΔSE) at the first resonant frequency is 20.4 dB and the frequency shift (Δf_{r1}) related to the first resonance position without and with absorber is 8 MHz, i.e., the first resonant frequency is shifted toward higher frequencies when the EMI absorber is placed inside.

Secondly, the measurement results for the SE of enclosure with the EMI absorbers placed on both side walls are compared to the empty enclosure case. It can be seen that the SE curves do not differ in terms of shape in whole frequency range, see Fig. 7, but the SE levels are different at resonant frequencies around 700 MHz, 1100 MHz and 1650 MHz, respectively. It can be observed a very good absorber efficiency at lower frequencies, while it is weaker at higher frequencies in observed range. Since a very thin EMI absorber is used, the additional TE and/or TM modes are not introduced inside enclosure. The respective SE level difference between compared cases is 23.65 dB, while the frequency shift of the first resonance, Δfr_1, is 8 MHz.

Further, the EMI absorbers are placed at the same time on the wall opposite to the front wall with an aperture and on both side walls of enclosure. The measured SE results are compared to the empty enclosure case in Fig. 8. For this case, the highest SE values are obtained at resonant frequencies of enclosure. The difference between the SE levels (ΔSE) at the first resonance for this case and the case of empty enclosure is 26.5 dB, while the first resonant frequency shift, Δfr_1, is 10 MHz. Again, at higher frequencies, the insertion of absorbers for this case led to the decrease of the SE, as depicted in Fig. 8.

Finally, Fig. 9 presents the zoomed view of the SE around the first resonant frequency for all considered positions of EMI absorber. It can be observed that the SE enhancement is achieved for every position of absorber inside. Moreover, the more absorbers are placed inside the enclosure on different walls, the more significant improvement in the level of the SE characteristics is obtained, especially at the first resonant frequency.

Table II summarizes the measured values of the SE at the first resonant frequency as well as the relative shift of this resonance and SE difference from the case of enclosure without absorber. Definitely, the most prominent frequency shift is obtained for the third case, see Fig. 9. The highest SE value of 11.55 dB at the first resonant frequency is achieved for the case with three absorbers giving the difference of 26.5 dB compared to the SE of enclosure without absorber.

V. Conclusion

In this paper, the presence of the EMI absorber inside the metal enclosure has been considered from the viewpoint of the values of SE of enclosure at its resonant frequencies. The most significant improvement of SE value at the first resonant frequency is obtained for the case with absorbers on the back wall and two side enclosure walls. However, it should be taken into consideration that the EMI absorber presence may also reduce the SE peaks at the higher frequencies in observed frequency range.

Future work will include the numerical analysis together with a developed numerical model of used absorbers, to support the experimental study conducted here. Based on simulated distribution of the EM field inside the enclosure, it would be possible to determine the optimal position of the absorbers inside that can increase the protective function of enclosure at resonant frequencies but also keep its high SE values at other frequencies.

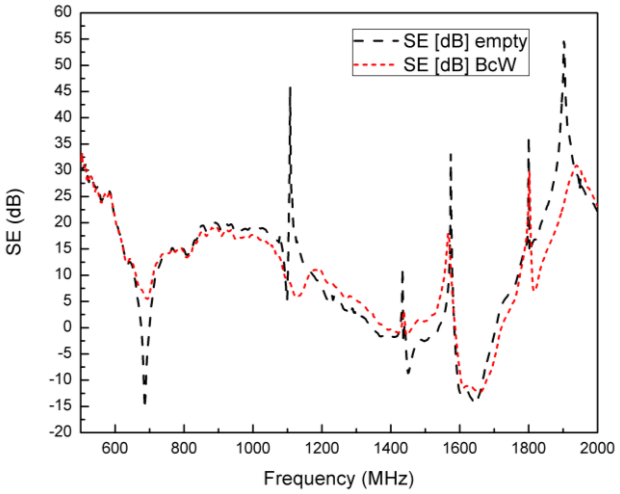

Fig. 6. The measurement results for the SE of the enclosure with the absorber placed on the wall on opposite side from frontal enclosure wall (case BcW).

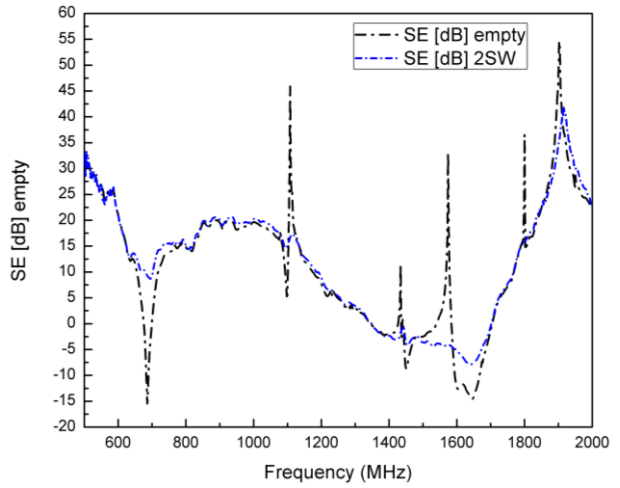

Fig. 7. The measurement results for the SE of the enclosure with the absorber placed on both side walls (case 2SW).

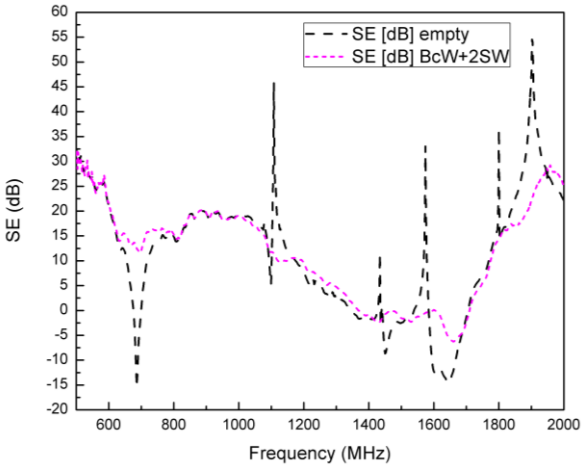

Fig. 8. The measurement results for the SE of the enclosure with the absorber placed on the wall on opposite side to the frontal wall and on both side walls (case BcW+2SW).

ACKNOWLEDGMENT

This work has been supported by the EUROWEB+ project, by the COST IC 1407 and by the Ministry of Education, Science and Technological Development of Republic of Serbia (Grant No. 451-03-9/2021-14/200102).

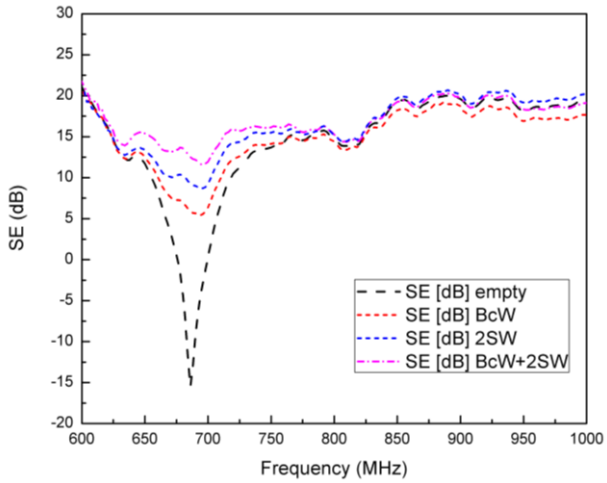

Fig. 9. The measurement results for the SE of enclosure, with the absorber inside, around the first resonant frequency (all three cases).

TABLE II
THE SE VALUES AT THE FIRST RESONANCE OF ENCLOSURE

EMI absorber position	***fr1_meas* [MHz]**	***SE_meas* [dB]**	***Δfr_meas* [MHz]**	***ΔSE_meas* [dB]**
BcW	694	5.45	8	20.4
2SW	694	8.70	8	23.65
BcW+2SW	696	11.55	10	26.5
Empty	686	-14.95	-	-

REFERENCES

[1] C. Christopoulos, The Transmission-Line Modelling (TLM) Method, New Jersey: *IEEE Press in assoc. with Oxford University Press*, Piscataway, 1995.

[2] X. Luo and D. D. Chung, "Electromagnetic interference shielding using continuous carbon-fiber carbon-matrix and polymer-matrix composites," *Elsevier Science: Composites: Part B*, vol. 30, pp. 227–231, 1999.

[3] R. Kumar, S. R. Dhakate, P. Saini and R. B. Mathur, "Improved electromagnetic interference shielding effectiveness of light weight carbon foam by ferrocene accumulation," *The Roy. Soc. of Chem*. 2013: *RSC Advances*, vol. 3, pp. 4145-4153, 2013.

[4] N. Nešić, B. Milovanović, N. Dončov, V. Mandrić-Radivojević and S. Rupčić, "Improving Shielding Effectiveness of a Rectangular Metallic Enclosure with Aperture by Using Printed Dog-bone Dipole Structure," *52nd ICEST*, pp. 97-100, Niš, Serbia, June 28-30, 2017.

[5] Nataša Nešić, Bratislav Milovanović, Nebojša Dončov, Vanja Mandrić-Radivojević, Slavko Rupčić, "Improving Shielding Effectiveness of a Metallic Enclosure at Resonant Frequencies", *13th TELSIKS*, Niš, October 2017, pp. 42-45, ISBN: 978-1-5386-1798-4 (IEEE).

[6] N. J. Nešić and N. S. Dončov, "Shielding Effectiveness Estimation by using Monopole-receiving Antenna and Comparison with Dipole Antenna," *Frequenz DeGruyter*, no.5-6, pp. 1-11, 2016.

[7] N. J. Nešić "Numerical and experimental analysis of aperture arrays impact on the shielding effectiveness of metal enclosures in microwave frequency range", *Doctoral thesis, in Serbian, Singidunum University*, Belgrade, 2017.

[8] https://multimedia.3m.com/mws/media/960654O/3m-emi-absorber-ab7000hf-series-halogen-free.pdf

[9] N. Nešić, S. Rupčić, V. Mandrić-Radivojević, N. Dončov, "Experimental analysis of a metal enclosure shielding effectiveness improvement with EMI absorber", paper accepted for publication on *15th Conference on Applied Electromagnetics, IIEC 2021*, Niš, Serbia.

Incorporating a Lowpass Filter into a Very Wide Bandpass Filter to Suppress Harmonics

Dušan Nešić, *Member, IEEE*

***Abstract*—This paper presents an algorithm for suppression of higher harmonics in response of the very wide bandpass filter (WBPF). Lowpass filter (LPF) is incorporated into the very wide bandpass filter to suppress harmonics. The LPF is consists of only three identical cells with uniform open stubs. At least two higher harmonics are suppressed.**

***Index Terms*— Microwaves, Suppression of higher harmonics for very wide bandpass filter, Ideal model.**

I. Introduction

ONE disadvantage of common bandpass filters is existing of higher harmonicas causing a narrow bandstop region on higher frequencies outside bandpass. This is specially a problem for the very wide bandpass filter (WBPF) like one presented in [1]. Common solution is incorporating lowpass filter (LPF) into the WBPF [2,3]. The solution intends not to significantly degrade bandpass characteristics but suppress higher harmonics. In the same time slow-wave characteristic of the lowpass filter shortens (minimizes) the structure. Problems can be nonuniform open stubs in [2] or too many different uniform open stubs like in [3].

Starting WBPF is from reference [1] with 150 % relative bandwidth. Ideal transmission structure and its response are presented in Fig. 1 and Fig. 2 in program package WIPL-D [4]. As can be seen in Fig. 2, bandstop region between the first bandpass and the next harmonic is narrow.

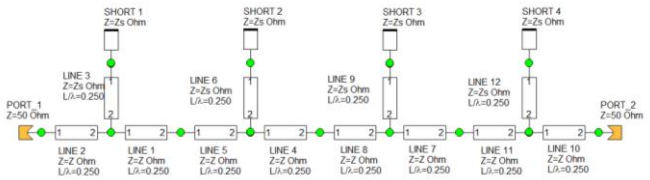

Fig. 1. Model of the ideal bandpass filter for relative bandwidth 150 %, presented in [1].

The aim is to suppress at least one higher harmonic. From Fig. 1 can be seen that transmission line segments between shorted stubs are λ/2 (2 x 0.250 λ), in phase π. To incorporate lowpass filter, the segment between the second and the third shorted stub is replaced with a lowpass filter. An example of a lowpass filter is chosen from [5]. It can be constructed of identical cells.

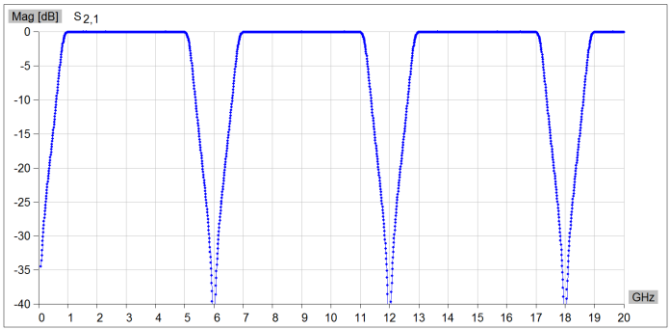

Fig. 2. S_{21} parameters for the filter around 3 GHz in the Fig. 1 with higher harmonica.

II. The Method

The method of incorporation of the lowpass filter is presented in Fig. 3. Instead of a transmission line segment π (λ/2 = 2 x 0.250 λ in upper Fig.3) between shorted stubs there are three equal cells of the lowpass filter, each with (*L1* + *L1*)* λ distance on the main line (3 x (*L1* + *L1*)* λ) in down Fig. 3). The phase difference π/3 is replaced with a cell presented in Fig. 4 with (*L1* + *L1*)* λ distance on the main line.

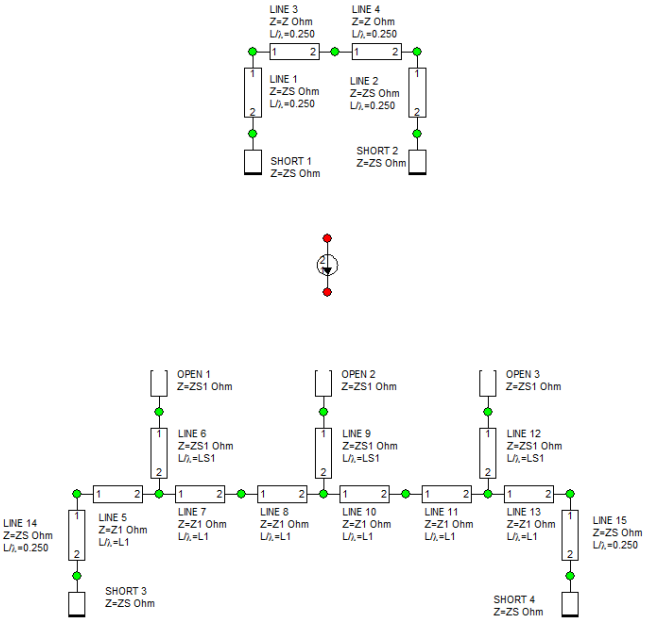

Fig. 3. Equivalence for incorporating low pass filter into bandpass filter.

Dušan Nešić is with Centre of Microelectronic Technologies, Institute of Chemistry, Technology and Metallurgy, University of Belgrade, Njegoševa 12, 11000 Belgrade, Serbia (E-mail: nesicad@nanosys.ihtm.bg.ac.rs).

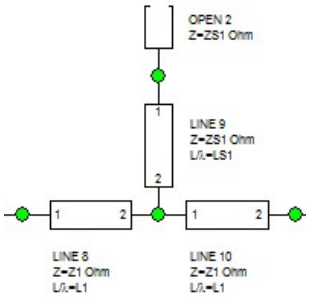

Fig. 4. One cell of the incorporated lowpass filter.

$A_cB_cC_cD_c$ matrix for the section $\pi/3$ of the primary filter with characteristic impedance *Z*, Fig. 1, is equaled on central frequency at 3 GHz with calculated ADCD matrix of the cell in Fig. 4. *L1* in Fig. 4 corresponds to phase difference *t1*, $L1 = t1/(2\pi)$. *Z1* is characteristic impedance of the main line and *ZS1* is characteristic impedance of the open stub. *LS1* corresponds to phase *tS1* of the open stub, $LS1 = tS1/(2\pi)$.

Calculation process is presented in Fig. 5 according to the reference [5], $Y = C_s/A_s$. Entering parameters are *Z*-characteristic impedance of the primary filter, *ZS*-characteristic impedance of the shorted stub of the primary filter (not in calculation, only in final results), *ZS1*-characteristic impedance of the open stub. *tS1*- phase length of the open stub was firstly treated as an entering parameter but later it is equaled with *t1* to get better response of the lowpass filter according to [5]. Output parameters are *t1* (*L1*) and *Z1*.

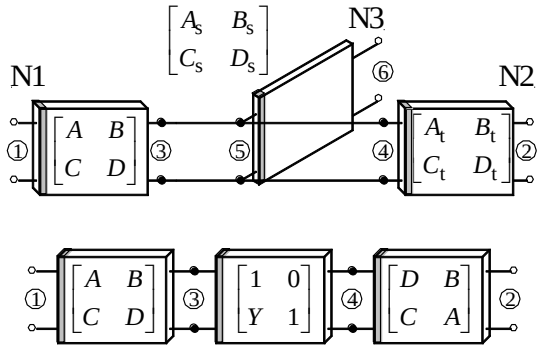

Fig. 5. Transformation of the cell in the Fig. 1 via ABCD matrix according to [4].

Equaled elements of matrix are presented in (1)-(3).

$$A_c(\pi/3) = \cos(\pi/3) = D_c(\pi/3) = AD + BC + BC_s\frac{D}{A_s} \quad (1)$$

$$B_c(\pi/3) = jZ\sin(\pi/3) = 2AB + C_s\frac{B^2}{A_s} \quad (2)$$

$$C_c(\pi/3) = j\sin(\pi/3)/Z = 2CD + C_s\frac{D^2}{A_s} \quad (3)$$

The corresponding ABCD-parameters for the cell in Fig. 4 are: $A = D = \cos(t1)$, $A_s = \cos(tS1)$, $B = \mathrm{j}Z1\sin(t1)$, $C = \mathrm{j}\sin(t1)/Z1$ and $C_s = \mathrm{j}\sin(tS1)/ZS1$.

Solution for *Z*1 from (1) and from (3) are (4) and (5) respectively

$$Z1 = \frac{ZS1\cdot(2\cos(2\cdot t1)-1)}{\sin(2\cdot t1)\cdot tg(tS1)} \quad (4)$$

$$Z1 = \frac{\sin(2\cdot t1)}{(\sqrt{3}/(2\cdot Z) - (\cos(t1))^2\cdot tg(tS1)/ZS1)} \quad (5)$$

Next, equal solutions from (4) and (5). After rearranging

$$(\cos(t1))^2 = 3\sqrt{3}/(4\sqrt{3} - 2Z(tg(tS1)/ZS1)) = C \quad (6)$$

$$t1 = a\cos(\sqrt{C}) \quad (7)$$

Return (5) to solution for *Z*1 and calculate *Z*1. Calculation in WIPL-D Microwave Pro v5.1 [4] is presented in Fig. 6. *Z*1 is firstly calculated via (6) and then checked via (5) (*PU*).

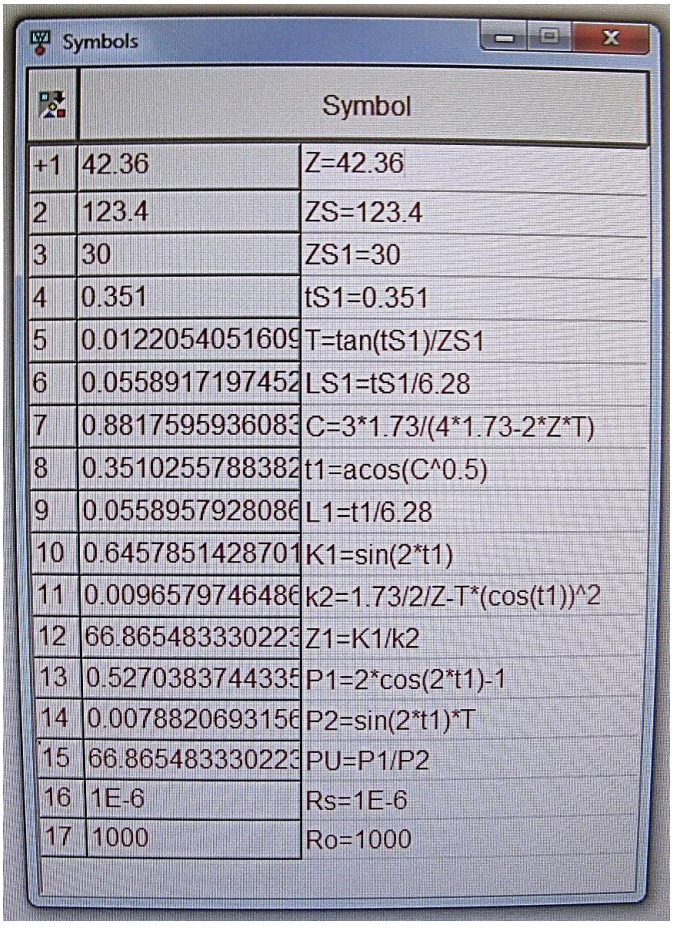

Fig. 6. Calculation of parameters in WIPL-D Microwave Pro v5.1. *T*=tg(*tS1*)/*ZS1*. PU only checks calculation.

III. Results

Entering values for *Z* and *ZS* are chosen according to [1] for the very wide bandpass filter with relative bandwidth of 150

% around 3 GHz. The value of characteristic impedance of the open stub, *ZS1*, is chosen to induce equality of *tS1* and *t1* for better characteristics of the lowpass filter [5].

The values from Fig. 6 are incorporated into models in Fig. 7. The final filter is symmetrical as can be seen in Fig. 7. Additional resistivity is incorporated to suppress numerical problems, Fig. 6. Results for S_{21} and S_{11} for the final structure with the incorporated lowpass filter are presented in Fig. 7. More than two higher harmonics are suppressed. S_{11} is below -15 dB in the bandpass.

IV. CONCLUSION

The algorithm for incorporating lowpass filter into bandpass is presented. For example, it is applied to a very wide bandpass (WBPF) filter of 150 %. Such WBPF has narrow bandstop and wide higher harmonic that make problems in circuits. More than two higher harmonics are suppressed with incorporated lowpass filter. The lowpass filter consists of only three identical cells with uniform arms in the middle of the WBPF structure. The algorithm is applicable to other bandpass filters. Further research will include simulation and fabrication in microstrip.

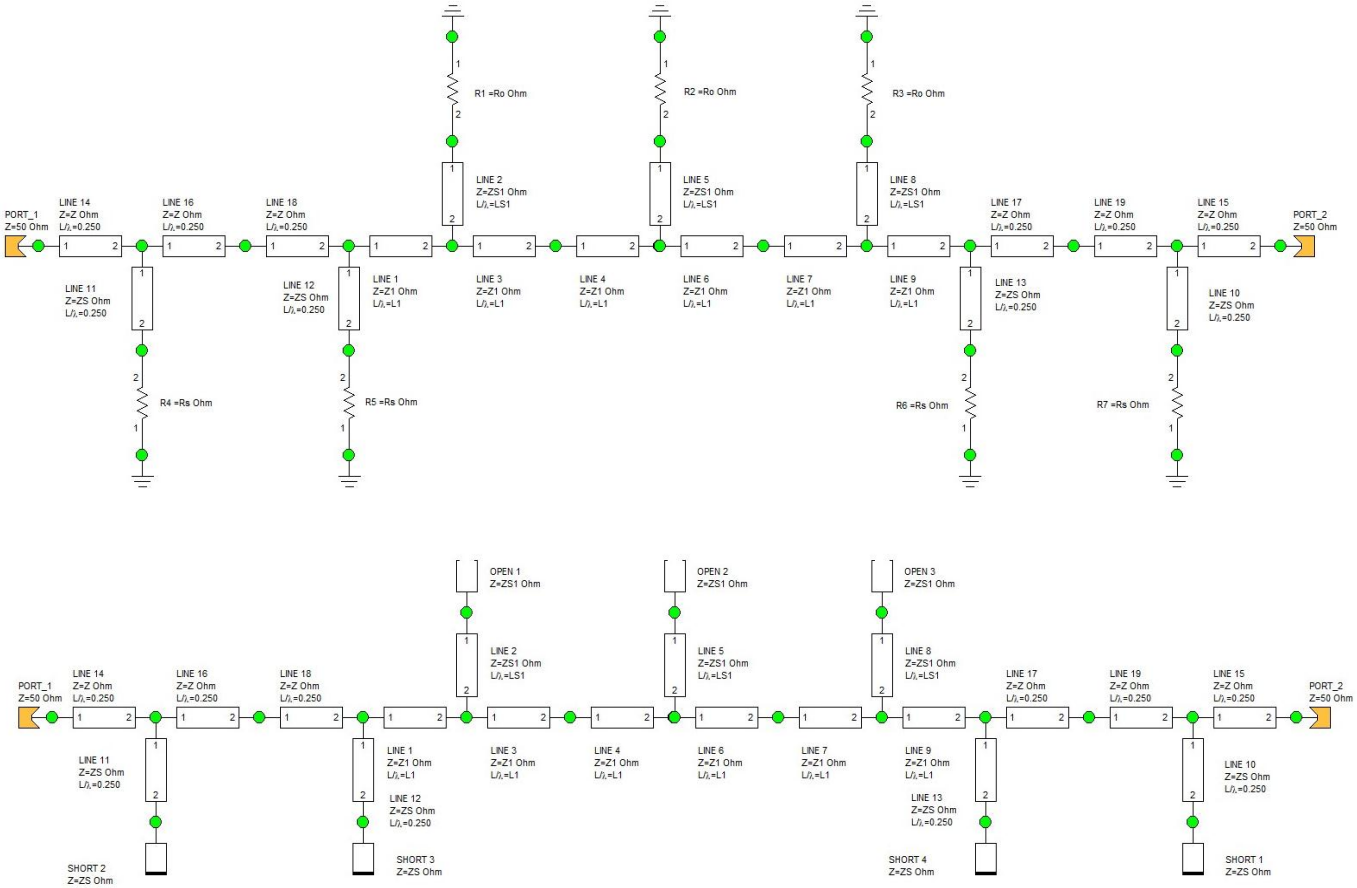

Fig. 7. Model of the lowpass filter incorporated into the bandpass filter, down model; the model with additional resistivity, upper model.

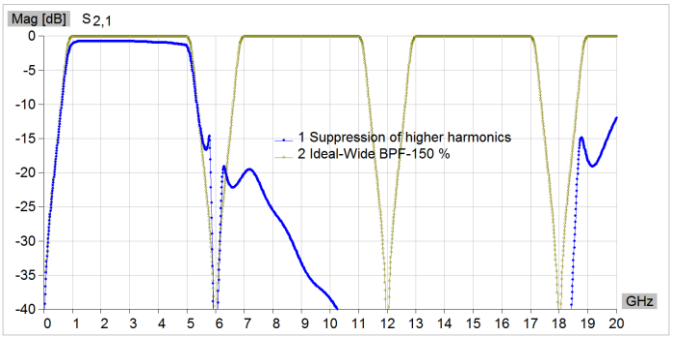

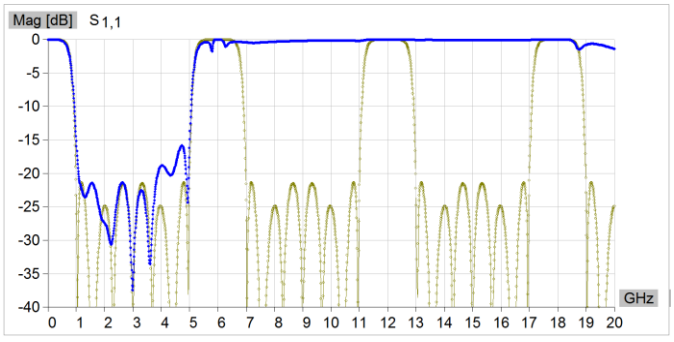

Fig. 8. S_{21} and S_{11} parameters for the resulting bandpass filter for *ZS1*-characteristic impedance of the open stub, equals 30 Ω.

ACKNOWLEDGMENT

This work was financially supported by Ministry of Education, Science and Technological Development of the Republic of Serbia (Grant No. 451-03-68/2020-14/200026).

REFERENCES

[1] D. Nesic, B. Kolundzija and T. Milosevic, "Simulation of wideband bandpass filters with arbitrary relative bandwidth," *7th International Conference on Electrical, Electronic and Computing Engineering, IcETRAN 2020*, API1.8 (MTI)

[2] J. García-García, J. Bonache, and F. Martín, Application of Electromagnetic Bandgaps to the Design of Ultra-Wide Bandpass Filters with Good Out-of-Band Performance, *IEEE Transactions on Microwave Theory and Techniques*, Vol. 54, No. 12, 2006, DOI 10.1109/TMTT.2006.886155, pp. 4136-4140

[3] K.-K. Ryu, Bandpass Filter Using Short Stubs and Step Impedances Lines for Ultra-Wideband Applications, *Microwave and Optical Technology Letters*, Vol. 53, No. 5, 2011, DOI 10.1002/mop, pp. 1062-1065

[4] *Program Package* WIPL-D Microwave Pro v5.1 (*WIPL-D d.o.o, Belgrade 2019*. www.wipl-d.com)

[5] D. A. Nesic, B. M. Kolundzija, D. V. Tosic and D. S. Jeremic, Low-pass filter with deep and wide stop band and controllable rejection bandwidth, *International Journal of Microwave and Wireless Technologies*, Vol. 7, Iss. 2, 2015, pp. 141-149